BAMS Article

Cyclogenesis in the Tropical Atlantic

First Scientific Highlights from the Clouds–Atmospheric Dynamics–Dust Interactions in West Africa (CADDIWA) Field Campaign

Cyrille Flamant, Jean-Pierre Chaboureau, Julien Delanoë, Marco Gaetani, Cédric Jamet, Christophe Lavaysse, Olivier Bock, Maurus Borne, Quitterie Cazenave, Pierre Coutris, Juan Cuesta, Laurent Menut, Clémantyne Aubry, Angela Benedetti, Pierre Bosser, Sophie Bounissou, Christophe Caudoux, Hélène Collomb, Thomas Donal, Guy Febvre, Thorsten Fehr, Andreas H. Fink, Paola Formenti, Nicolau Gomes Araujo, Peter Knippertz, Eric Lecuyer, Mateus Neves Andrade, Cédric Gacial Ngoungué Langué, Tanguy Jonville, Alfons Schwarzenboeck, and Azusa Takeishi

KEYWORDS:
Tropical cyclones; Storm environments; Aircraft observations; Aerosol radiative effect; Aerosol-cloud interaction

ABSTRACT: During the boreal summer, mesoscale convective systems generated over West Africa propagate westward and interact with African easterly waves, and dust plumes transported from the Sahel and Sahara by the African easterly jet. Once off West Africa, the vortices in the wake of these mesoscale convective systems evolve in a complex environment sometimes leading to the development of tropical storms and hurricanes, especially in September when sea surface temperatures are high. Numerical weather predictions of cyclogenesis downstream of West Africa remains a key challenge due to the incomplete understanding of the clouds–atmospheric dynamics–dust interactions that limit predictability. The primary objective of the Clouds–Atmospheric Dynamics–Dust Interactions in West Africa (CADDIWA) project is to improve our understanding of the relative contributions of the direct, semidirect, and indirect radiative effects of dust on the dynamics of tropical waves as well as the intensification of vortices in the wake of offshore mesoscale convective systems and their evolution into tropical storms over the North Atlantic. Airborne observations relevant to the assessment of such interactions (active remote sensing, in situ microphysics probes, among others) were made from 8 to 21 September 2021 in the tropical environment of Sal Island, Cape Verde. The environments of several tropical cyclones, including Tropical Storm Rose, were monitored and probed. The airborne measurements also serve the purpose of regional model evaluation and the validation of spaceborne wind, aerosol and cloud products pertaining to satellite missions of the European Space Agency and EUMETSAT (including the Aeolus, EarthCARE, and IASI missions).

https://doi.org/10.1175/BAMS-D-23-0230.1
Corresponding author: Cyrille Flamant, cyrille.flamant@latmos.ipsl.fr
Supplemental material: https://doi.org/10.1175/BAMS-D-23-0230.2
In final form 27 December 2023

AFFILIATIONS: Flamant, Delanoë, Cazenave, Aubry, Bounissou, Caudoux, Collomb, and Jonville—Laboratoire Atmosphères, Milieux, Observations Spatiales, UMR 8190, CNRS, Sorbonne Université and Université Paris Saclay, Paris, France; **Chaboureau and Takeishi**—Laboratoire d'Aérologie, UMR 5560, Université de Toulouse, CNRS, UT3, IRD, Toulouse, France; **Gaetani**—Scuola Universitaria Superiore IUSS, Pavia, Italy; **Jamet**—Laboratoire d'Océanologie et de Géosciences, UMR 8187, Université Littoral Côte d'Opale, CNRS, Université de Lille, IRD, Wimereux, and Laboratoire Atmosphères, Milieux, Observations Spatiales, UMR 8190, CNRS, Sorbonne Université and Université Paris Saclay, Paris, France; **Lavaysse**—Institut des Géosciences de l'Environnement, UMR 5501, Université Grenoble Alpes, CNRS, IRD, G-INP, Grenoble, France, and Joint Research Centre, European Commission, Ispra, Italy; **Bock**—Institut de physique du globe de Paris, UMR 7154, Université de Paris, CNRS, IGN, Paris, and Ecole Nationale des Sciences Géographiques-Géomatique, IGN, Marne-la-Vallée, France; **Borne, Fink, and Knippertz**—Institute of Meteorology and Climate Research, Karlsruhe Institute of Technology, Karlsruhe, Germany; **Coutris, Febvre, and Schwarzenboeck**—Laboratoire de Météorologie Physique, UMR 6016, Université Blaise Pascal, CNRS, Clermont-Ferrand, France; **Cuesta**—Univ Paris Est Creteil and Université Paris Cité, CNRS, LISA, Créteil, France; **Menut**—Laboratoire de Météorologie Dynamique, UMR 8539, École Polytechnique, Université Paris Saclay, ENS, IPSL Research University, Palaiseau, France; **Benedetti**—Earth System Predictability Section, European Centre for Medium-Range Weather Forecasts, Reading, United Kingdom; **Bosser**—Laboratoire des sciences et technologies de l'information, de la communication et de la connaissance, UMR 6285, CNRS, ENSTA-Bretagne, Brest, France; **Donal**—Ecole Nationale des Sciences Géographiques-Géomatique, IGN, Marne-la-Vallée, France; **Fehr**—Directorate of Earth Observation Programmes, European Space Research and Technology Centre, Noordwijk, Netherlands; **Formenti**—Université Paris Cité and Univ Paris Est Creteil, CNRS, LISA, Paris, France; **Araujo and Andrade**—Faculdade de Ciências e Tecnologia, University of Cape Verde, Praia, Cape Verde; **Lecuyer**—Laboratoire d'Océanologie et de Géosciences, UMR 8187, Université Littoral Côte d'Opale, CNRS, Université de Lille, IRD, Wimereux, France; **Langué**—Laboratoire Atmosphères, Milieux, Observations Spatiales, UMR 8190, CNRS, Sorbonne Université and Université Paris Saclay, Paris, and Institut des Géosciences de l'Environnement, UMR 5501, Université Grenoble Alpes, CNRS, IRD, G-INP, Grenoble, France

During the boreal summer over Africa north of the equator, the gradient of temperature between the heated land and the ocean generates a monsoon flow in the lower troposphere that peaks in late August, bringing moisture to the Sahel and favoring deep convection. The convergence of the harmattan and the monsoonal flow shapes the synoptic-scale circulation near the surface over the continent. In the midtroposphere and around 15°N, the thermal gradient between the hot and dry air above the Sahara and the cooler and moister air above the Guinea Coast drives the African easterly jet (AEJ), which is a key feature of the West African monsoon (WAM) system. This time of year is also propitious to the emission and westward transport of terrigenous aerosol (also generally referred to as dust) from a number of sources scattered across the Sahara and the Sahel. Emissions are related to a variety of near-surface dynamical processes such as low-level jets (Washington and Todd 2005) and gusty fronts (e.g., the intertropical discontinuity marking the monsoon–harmattan interface, or convective cold pools emanating from deep convection; Flamant et al. 2007; Bou Karam et al. 2008). In particular, the cold pools originating from mesoscale convective systems (MCSs; Houze 2004), i.e., large organized convective storms traveling westward across the continent, are effective dust mobilizers accounting for a large part of the emissions over

West Africa (Marsham et al. 2011; Kocha et al. 2013). African easterly waves (AEWs; Burpee 1972) developing along the AEJ also contribute to accelerating the northward propagation of the intertropical discontinuity on a daily basis, thereby enhancing dust emission (Knippertz and Todd 2010, 2012; Cuesta et al. 2020).

Terrigenous aerosols emitted from the Sahara and Sahel, in turn, affect the atmospheric dynamics and meteorology over West Africa and the tropical North Atlantic (Lavaysse et al. 2011; N'Datchoh et al. 2018), through the so-called aerosol direct and semidirect effects (surface cooling and midtroposphere heating, respectively), which act on atmospheric stability (e.g., Ramanathan et al. 2007; Zhao et al. 2010). They also influence precipitation associated with MCSs over West Africa due to their capacity to act as cloud condensation and ice nuclei (so-called aerosol indirect effect; DeMott et al. 2003; Yin and Chen 2007; Zhao et al. 2011; Price et al. 2018) as well as due to the semidirect aerosol effect (Reinares-Martínez and Chaboureau 2018). Hence, the atmospheric circulation over West Africa driving the westward transport of dust and MCSs over the adjacent Atlantic Ocean is the result of intricate processes involving complex aerosol–radiation–cloud interactions.

Over the ocean, downstream of West Africa, the remains of continental MCSs evolve in the complex coastal environment and interact with the atmospheric circulation (AEJ and tropical waves), the upper oceanic layer and the terrigenous aerosols advected within the Saharan air layer (SAL), an elevated layer of Saharan air crossing the North Atlantic (Carlson and Prospero 1972; Karyampudi et al. 1999; Dunion and Velden 2004, among others). Tropical wave phenomena of interest in this part of the globe are Kelvin waves, equatorial Rossby waves, mixed Rossby–gravity waves, the Madden–Julian oscillation, and tropical disturbances including AEWs. This complex dynamical and compositional environment offshore of West Africa is sometimes favorable to the formation of tropical cyclones (TCs). For instance, developing AEWs (those strengthening as they travel westward and in which well-organized deep convection is collocated with the AEW trough) are known to be primary precursors of TCs (Pasch et al. 1998; Thorncroft and Hodges 2001; Dieng et al. 2017), accounting for ~60% of tropical storms (Russell et al. 2017) and 85% of major hurricanes (Landsea 1993), occasionally as far east as near Cape Verde (e.g., Jenkins et al. 2017). On the other hand, developing AEWs only represent a small fraction of AEWs leaving the West African coast (Hopsch et al. 2010; Arnault and Roux 2011). The SAL also affects the evolution of AEWs (Zipser et al. 2009) and the generation of TCs (Evan et al. 2006; Jenkins et al. 2008; Jenkins and Pratt 2008). Even after genesis, dust can significantly affect TC tracks and evolution because of aerosol radiative effects (Chen et al. 2015; Nowottnick et al. 2018) and through modifications in the TCs microphysics (Zipser et al. 2009; Luo and Han 2021). Although all the processes linking dust outbreaks to TC genesis are not yet fully understood, several studies suggest that dust outbreaks are anticorrelated to TC activity (e.g., Dunion and Velden 2004; Reed et al. 2019). Other studies have suggested indeterminant influences (Braun 2010) or positive influences of dust (Karyampudi and Carlson 1988; Karyampudi and Pierce 2002; Herbener et al. 2014) on TCs.

Background and motivation

Currently, interactions between dust, atmospheric dynamics, and clouds in West Africa and the tropical North Atlantic are very poorly accounted for in numerical weather prediction (NWP) models. This likely impairs an improvement in understanding and forecasting the development of intense storms and TCs over the North Atlantic. For instance, Vogel et al. (2018) have shown that NWP models have very low skills in tropical Africa for three main reasons. First, tropical Africa is characterized by the largest degree of mesoscale convective organization worldwide, a challenge for NWP convection schemes (Becker et al. 2021). Second, current NWP models struggle to reproduce the coupling between tropical waves and

the mean atmospheric flow as well as with the advection of dust and MCSs, possibly due to dust-induced effects in the wave development (Jones et al. 2004; Grogan et al. 2019; Nathan et al. 2019; Jury and Santiago 2010). Third, observational networks are very scarce over West Africa, thereby stressing the need for fully validated satellite products to be available over the region for assimilation in NWP model.

TCs pose a threat to human lives as well as the economy and the environment of impacted regions along their tracks. Due to their high population and asset density, and to its location at the end of the climatological North Atlantic cyclone track, the Caribbean and North American Atlantic coasts are particularly exposed. For instance, according to the National Oceanic and Atmospheric Administration (NOAA), the damages of all TCs between 1980 and 2020 amount to more than one trillion dollars in the United States only (NOAA 2021), while Mitch, one of the deadliest hurricanes to hit Central and North America, claimed more than 11,000 lives in 1998. Landsea (2015) highlighted that, since the early 1970s, about 25% of all Atlantic basin hurricanes struck the continental United States.

Even though the 3-day forecast error on cyclone tracks has been dramatically reduced in the past decades [from 300 to 100 nautical miles (n mi; 1 nm = 1.852 km) between 1990 and 2016; Landsea and Cangialosi 2018] there is still no general theoretical framework that can provide a thorough explanation for TC occurrence, thereby limiting their predictability. Models still fail to correctly forecast ~54% of cyclogenesis with a 5-day lead time, and ~30% with a 3-day lead time (Liang et al. 2021). Errors in initial intensity often propagate in the model and lead to bad cyclone intensity forecast (Emanuel and Zhang 2016). Therefore, the early development stage of TCs is still an active field of research. Enhanced knowledge of aerosol–cloud–dynamics interactions in the eastern part of the tropical North Atlantic is key to better understanding and forecasting of intense storm development over the North Atlantic. For that purpose, new, more comprehensive observations are needed over sea adjacent to West Africa.

To tackle this ambitious challenge, a consortium of European and U.S. scientists concerned with improving knowledge on cyclogenesis in the tropical North Atlantic have joined forces and built a cooperative program, including an international campaign that took place in September 2021 together with the European Space Agency (ESA) and the National Aeronautics and Space Administration (NASA), namely, the Joint Aeolus Tropical Atlantic Campaign (JATAC; Fehr et al. 2021). JATAC involved four aircraft, as well as one boat and several ground-based sites (see online supplementary material; https://doi.org/10.1175/BAMS-D-23-0230.2). The Clouds–Atmospheric Dynamics–Dust Interactions in West Africa (CADDIWA) project is one component of JATAC, with a major overlap in scientific goals with all the other JATAC elements (i.e., enhanced comprehension of the 2021 TC season through the acquisition of an innovative combination of new observations and high-resolution modeling). It also has specific scientific objectives within that common goal, as detailed in the following.

CADDIWA scientific objectives

Cape Verde is located immediately downstream of the massive dust plumes from the Sahel and the Sahara that exit the African continent in August and September while being advected westward by the easterly flow between 1.5 and 4 km above mean sea level (MSL). Cape Verde is also ideally located to monitor significant weather phenomena, such as the remains of continental MCSs as they evolve in the complex coastal environment and interact with the atmospheric circulation (the AEWs notably; Arnault and Roux 2011), the ocean, and the dust. Nevertheless, out of the campaigns conducted in the area, only a few considered dust–dynamics interactions.

The data gathered over the eastern Atlantic Ocean during the Global Atmospheric Research Program (GARP) Atlantic Tropical Experiment (GATE) near Cape Verde in 1974

(Reed et al. 1977) consolidated the pioneering work conducted in the early 1960s on the role of AEWs as seedlings for TCs over the North Atlantic. The interactions between AEWs, the SAL, and TCs have been investigated during the NASA African Monsoon Multidisciplinary Analysis (NAMMA; Jenkins et al. 2008; Jenkins and Pratt 2008; Zipser et al. 2009), which took place in Cape Verde as part of a broader collaborative effort across West Africa known as AMMA (Redelsperger et al. 2006). Several cases of developing and nondeveloping AEWs off the coast of West Africa have been analyzed by Arnault and Roux (2009, 2010a,b, 2011), while others concentrated on the formation of Hurricane Helene (Schwendike and Jones 2010; Chen et al. 2015; Folmer et al. 2016). Terrigenous aerosols have been extensively studied in the vicinity of Cape Verde during dedicated campaigns such as the Saharan Dust Experiment (SHADE; Tanré et al. 2003), Dust Outflow and Deposition to the Ocean (DODO; McConnell et al. 2008), Saharan Mineral Dust Experiment (SAMUM-2; Ansmann et al. 2011) and Saharan Aerosol Long-range Transport and Aerosol–Cloud-Interaction Experiment (SALTRACE; Weinzierl et al. 2017), Aerosol Properties–Dust (AER-D; Ryder et al. 2018), or using ground-based lidar measurements in the Cape Verde region (Ansmann et al. 2009, 2011). The Hurricane and Severe Storm Sentinel (HS3) mission (Braun et al. 2016) aimed to improve understanding of the physical processes that control intensity change of TCs across the northern Atlantic, focusing on the relative roles of environmental (including the dust-laden SAL) and inner-core processes. More recently, interactions between tropical waves and deep convective systems were examined during the Ice in Clouds Experiment–Dust field campaign (ICE-D; Price et al. 2018) based in Praia, Cape Verde.

Together with all the European components of the JATAC campaign, the CADDIWA field campaign was held in September 2021 in Cape Verde and comprised large airborne and ground-based detachments on the island of Sal, and a boatborne detachment on São Vicente.

The first overarching objective of the CADDIWA project is to assess dust direct, semidirect, and indirect effects on atmospheric dynamics in the complex coastal environment offshore of Senegal in different dust load conditions and in a variety of tropical wave–driven synoptic conditions, using a combination of observational and modeling approaches. The second overarching objective is to contribute to the calibration/validation (Cal/Val) of wind, cloud, and aerosol products of two space missions, namely, *Aeolus* (Stoffelen et al. 2005) and the Infrared Atmospheric Sounding Interferometer (IASI; Hilton et al. 2012) as well as ocean subsurface optical properties from *Aeolus*. It also aims to prepare the processing algorithms of the cloud and aerosol products of Earth Cloud, Aerosol, and Radiation Explorer (EarthCARE; Illingworth et al. 2015) and the wind retrievals of Wind Velocity Radar Nephoscope (WIVERN; Illingworth et al. 2018) using the in situ and remote sensing data gathered during the campaign. The third overarching objective is the validation of regional climate models and NWP models.

To achieve the CADDIWA goals, we gathered new observations pertaining to the assessment of dust direct, semidirect, and indirect effects as well as aerosol–cloud–dynamics interactions from dedicated ground-based and airborne platforms operating in the eastern tropical North Atlantic.

The CADDIWA campaign strategy

The CADDIWA contributions to the JATAC 2021 campaign are now described. They included a variety of instrumentation and assets that are summarized in Table 1.

Airborne campaign. The CADDIWA aircraft campaign was based on the deployment of the French Falcon 20 environmental research aircraft of Safire (Safire FA20) in the tropical

Table 1. CADDIWA instrumentation and assets. LATMOS = Laboratoire Atmosphères, Milieux, Observations Spatiales; LAERO = Laboratoire d'Aérologie; LOG = Laboratoire d'Océanologie et de Géosciences; LaMP = Laboratoire de Météorologie Physique; LMD= Laboratoire de Météorologie Dynamique; LISA = Laboratoire Interuniversitaire des Systèmes Atmosphériques; KIT = Karlsruher Institut für Technologie; IGN = Institut national de l'information géographique et forestière; Safire = Service des Avions Français Instrumentés pour la Recherche en Environnement; CLIMAT= Conveyable Low-noise Infrared radiometer for Measurements of Atmosphere and ground surface Targets; VSF = Volume scattering function; AC-S = Spectral absorption and attenuation sensor; WRF = Weather Research and Forecasting Model.

Instrument/asset	Description of parameters measured and/or derived	Resp. institution	Platform/ location
Rosemount T	Temperature	Safire	Safire FA20
Rosemount transducer 1221F	Pressure (static and dynamic)	Safire	Safire FA20
Buck Research CR2 and 1011C	Dewpoint temperature	Safire	Safire FA20
Litton 90–100 Inertial Navigation System + Trimble Global Positioning System + Collins	Wind components	Safire	Safire FA20
ADC 80 barometric altimeter + TRT AHV 8 radio altimeter	Aircraft position, attitude, altitude	Safire	Safire FA20
Vaisala Airborne Vertical Atmospheric Profiling System (AVAPS) dropsonde system	Temperature, humidity, and horizontal wind profiles between 11,000 m MSL and the surface	Safire	Safire FA20
CLIMAT radiometer	Brightness temperature in the IR (8.7, 10.8, and 12 μm); nadir pointing 0.16-s resolution	Safire	Safire FA20
Kipp and Zonen CMP22 (×2)	Upwelling and downwelling visible radiances and fluxes in the spectral range 0.2–3.6 μm 5-s resolution	Safire	Safire FA20
Kipp and Zonen CGR4 (×2)	Upwelling and downwelling IR radiances and fluxes in the spectral range 4.2–42 μm 0–700 W m^{-2} 5-s resolution	Safire	Safire FA20
Cloud droplet probe CDP	Cloud droplet spectrum (2–50 μm), 30 bins LWC, effective radius 1-s resolution	LaMP	Safire FA20
Two-dimensional stereo probe 2DS	Cloud particles spectrum (25–1,550 μm), 62 bins IWC and LWC, shape of particles 1-s resolution	LaMP	Safire FA20
Nevzorov probe	TWC (=IWC + LWC) 1-s resolution	Safire	Safire FA20
Forward-scattering spectrometer probe (FSSP)	Aerosol size distribution (275 nm–20 μm), 30 bins 1-s resolution	LaMP	Safire FA20
Ultrahigh-sensitivity aerosol spectrometer (UHSAS-A)	Aerosol size distribution (40 nm–1 μm), 100 bins 1-s resolution	LaMP and Safire	Safire FA20
LNG high-spectral-resolution aerosol/cloud Doppler lidar	Aerosol, cloud backscatter, and extinction coefficient at 355, 532, and 1,064 nm, HRS (including Doppler) at 355 nm, polarization at 355 nm operating at 20 Hz Nadir, zenith, and 37° off-nadir pointing 1-s resolution (adjustable)	LATMOS	Safire FA20
RASTA Doppler cloud radar	Radar reflectivity at 95 GHz, Doppler velocity along up to four different beams; from these measurements IWC, extinction, sea surface reflectivity, particle size, terminal fall speed, and the three wind components are retrieved (below aircraft) 250-ms resolution (adjustable)	LATMOS	Safire FA20
GNSS station	Total column water vapor	IGN	Sal, Cape Verde

(*Continued*)

Table 1. (*Continued*)

Instrument/asset	Description of parameters measured and/or derived	Resp. institution	Platform/ location
Radiosonde	Vertical profiles of temperature, humidity, wind	KIT	Sal, Cape Verde
TriOs radiometer	UV/VIS hyperspectral spectra of the water-leaving reflectance at the surface	LOG	Boat *Gamboa*
TriOs radiometer	UV/VIS hyperspectral spectra of the attenuation up to 30-m depth	LOG	Boat *Gamboa*
ECO-VSF WetLabs	VIS absorption and backscattering coefficients of the seawater up to 30 m	LOG	Boat *Gamboa*
AC-S WetLabs	Concentration of chlorophyll-a at 2-, 4-, 6-, 8-, 10-, 15-, and 20-m depth	LOG	Boat *Gamboa*
Niskin bottle	Particulate organic carbon at 4-, 6-, and 8-m depth	LOG	Boat *Gamboa*
Niskin bottle	Colored dissolved organic carbon at 2-m depth	LOG	Boat *Gamboa*
CADDIWA Operations Center	Daily meteorological and atmospheric composition forecast briefings, daily instrumentation status briefings, daily aircraft flights preparation briefings, daily JATAC coordination briefings	LATMOS	Sal, Cape Verde
WRF-CHIMERE regional model	Dedicated daily CADDIWA meteorological and atmospheric composition forecasts	LMD	Palaiseau, France
Meso-NH regional model	Dedicated twice-daily CADDIWA meteorological and atmospheric composition forecasts	LAERO	Toulouse, France
AEROIASI processing	Dedicated twice-daily processing of IASI instruments operating from platforms *MetOp-A*, *MetOp-B*, and *MetOp-C*: aerosol optical depth, aerosol extinction, and mean aerosol-layer height	LISA	Créteil, France

environment of Cape Verde, offshore of Senegal, from 8 to 21 September 2021. The Safire FA20 operated from the Amilcar Cabral International airport on Sal Island. Its payload was composed of in situ and remote sensing instruments and tailored to characterize atmospheric dynamics and thermodynamics as well as aerosol and clouds radiative and microphysical properties (Table 1). When relevant, the Safire FA20 flights were designed so to probe through active AEWs troughs associated with deep convection, as well as the pre- and poststorm environment and/or the front and back of AEWs troughs.

To achieve large synergies between science and Cal/Val objectives, the airborne data were acquired along *Aeolus* morning orbits (around 0730 UTC) and afternoon orbits (around 1930 UTC) in the vicinity of Sal, Cap Verde, as well as within the IASI/*MetOp-C* swath provided it covered Cape Verde (around 1115 UTC). Given the fairly limited range of the Safire FA20 (i.e., 1,400 n mi), a predefined calendar of flight plans was implemented based on the *Aeolus* ANX 2.0 orbit predictions, considering the proximity of the satellite tracks: the transit time needed to reach a given satellite orbit (and come back to Sal) should not exceed 50% of the time of flight of the Falcon 20.

During the campaign, selected flights dates enabled performing stacked legs along *Aeolus* orbits and around the satellite overpass time in order to conduct a proper assessment of the aerosol, clouds and atmospheric dynamics using the aircraft payload. At least one leg was made at the Safire FA20 ceiling altitude with the LEANDRE Nouvelle Generation (LNG; Bruneau et al. 2015) lidar pointing off-nadir with a 37° angle, i.e., in a geometrical configuration similar to the ALADIN lidar on board *Aeolus*, and the nadir-pointing antenna of the cloud Radar Airborne System (RASTA; Delanoë et al. 2013). A second leg was performed in the SAL as the aircraft flew under its own track, thereby allowing in situ characterization (cloud and aerosol microphysical probes) and nadir and/or zenith radar and lidar measurements where nadir active remote sensing observations were gathered along the high-level leg. In addition, vertical profiles of all dynamics, thermodynamics, and atmospheric composition were also obtained from dropsondes released while the aircraft was flying high, as well as during aircraft soundings (after take-off, before landing, and during flight level changes).

Table 2. Summary of Safire FA20 flights performed from Sal. Drops = dropsondes released during the flight. TP = tropical perturbation. TS = tropical storm. DLR F20 = Deutsches Zentrum für Luft- und Raumfahrt Falcon 20 aircraft operating from the Island of Sal. AA WT-10 = Aerovizija Advantic WT-10 aircraft operating from Mindelo (São Vicente Island, Cape Verde). Also see supplementary material for details on the JATAC components.

Date	Flight number	Time (UTC)	No. of drops	Objectives	Coordination with
8 Sep 2021	F5/fs21005	0636–0957	3	*Aeolus* west of Mindelo	DLR F20, AA WT-10
10 Sep 2021	F6/fs21006	1842–2223	5	*Aeolus* Mindelo overpass	DLR F20, AA WT-10, boat *Gamboa*
11 Sep 2021	F7/fs21007	0916–1243	10	TP Pierre Henri	
11 Sep 2021	F8/fs21008	1447–1756	8	TP Pierre Henri	AA WT-10
14 Sep 2021	F9/fs21009	0626–0924	6	*Aeolus* Sal overpass	AA WT-10
16 Sep 2021	F10/fs21010	1806–2116	6	*Aeolus* east of Sal	DLR F20, AA WT-10
17 Sep 2021	F11/fs21011	1834–2216	3	*Aeolus* Mindelo overpass	DLR F20, AA WT-10, boat *Gamboa*
18 Sep 2021	F12/fs21012	1603–1940	2	TS Rose	Boat *Gamboa*
19 Sep 2021	F13/fs21013	0906–1243	2	TS Rose	

The Safire FA20 performed nine flights covering 32 science hours and released 46 dropsondes. Five flights along *Aeolus* tracks (two morning orbits, three afternoon orbits, see Table 2 and flight tracks F5, F6, F9, F10, and F11 in Fig. 1) in mostly cloud-free conditions to document the Saharan air transport and contribute to *Aeolus* and IASI Cal/Val on wind and aerosol L2 products. The instruments on board the Safire FA20 most pertaining to the *Aeolus* and IASI Cal/Val objectives are listed in Table 3.

Not all CADDIWA flights were performed along *Aeolus* tracks, as one of our objectives was also to chase tropical disturbances in the early stage of their formation near Cape Verde to document their environment (dynamics, thermodynamics, and composition) and the convective cells present in the tropical wave troughs. Four flights in the environment of a tropical perturbation [TP; referred to as "Pierre Henri" in the following as it was not named nor numbered by the NOAA National Hurricane Center (NHC)] and TS Rose (flight tracks F7, F8, F12 and F13 in Fig. 1). This allowed documentation of aerosol–cloud–dynamics interactions and gather data for model validation purposes of TC precursors as well as to provide proxy data for EarthCARE cloud products development. Even though the Safire FA20 flew straight, leveled legs, this was not imposed by a satellite orbit or timing, but rather to facilitate the processing and analysis of the data. The remote sensing and in situ cloud and aerosol data gathered during these flights will serve for the preparation of the EarthCARE processing algorithms as well as for the WIVERN mission. The instruments on board the Safire FA20 most pertaining to the EarthCARE and WIVERN preparation objectives are listed in Table 3.

Aerosol in situ probes (UHSAS and SPP-300) were fully operational during all flights. The laser diode of the CPD probe (cloud droplets measurements) failed at the end of F7 making the probe inoperative during F8 (same day). A spare CDP probe was flown during F9 to F13. The 2DS probe (drizzle/rain drop and ice crystals) suffered from data losses due to communication instability in the Ethernet link between the probe and the data acquisition and control system. The issue happened in clear sky most of the time, with limited impact on in cloud data collection in all flights but F8 wherein cloud data are sparse. There were also issues with the dropsondes, especially during F6 and F8 related to the initialization procedure as the dropsondes did not pick up the GNSS signal in the aircraft. A new procedure has been developed in order to limit dropsondes problem from F11 onward which was based on a much longer initialization period (30 min) in the aircraft before launch. The RASTA

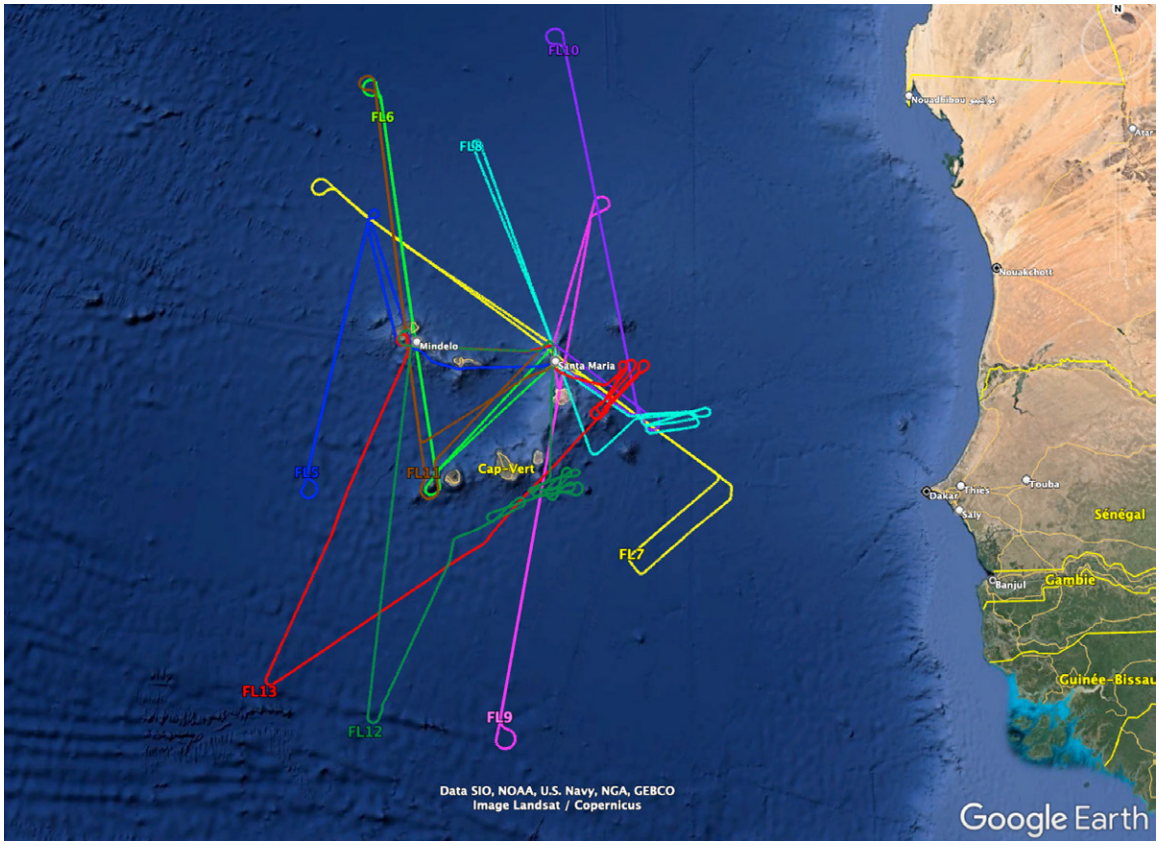

Fig. 1. Safire FA20 flight tracks for the nine flights conducted during the CADDIWA detachment in Cape Verde. Flights F5, F6, F9, F10, and F11 were made along *Aeolus* orbits. Flight F5 and F9 were conducted along morning orbits on 8 and 14 Sep, respectively. Flights F6, F10, and F11 were conducted along afternoon orbits on 10, 16, and 17 Sep, respectively. Flights F7 and F8 were made in the environment of Tropical Perturbation Pierre Henri on 11 Sep, and flights F12 and F13 in the environment of TS Rose on 18 and 19 Sep 2021. Map credit: Google Earth 2021.

radar, Safire baseline measurements, and CLIMAT worked perfectly during the whole time. The LNG lidar was operational most of the time, with only a few issues leading to small gaps in data. Due to saturation effect, the LNG data at 1,064 nm are only available when the lidar is pointing nadir.

Table 3. Safire Falcon 20 payload for CADDIWA and its relevance for *Aeolus* and IASI/*MetOp-C* Cal/Val as well as EarthCARE and WIVERN preparation activities.

	Spaceborne products															
	Aerosols				Clouds				Wind				Surface reflectivity			
Instrument	*Aeolus*	IASI-C	Earth-CARE	WIVERN	*Aeolus*	IASI-C	Earth-CARE	WIVERN	*Aeolus*	IASI-C	Earth-CARE	WIVERN	*Aeolus*	IASI-C	Earth-CARE	WIVERN
LNG	×	×	×		×		×		×		×					×
RASTA							×	×			×	×				×
Dropsondes									×		×	×				
CLIMAT	×	×					×	×								
Pyrano- and pyrgeometers	×	×					×	×								
UHSAS and FSSP	×	×	×													
CDP and 2DS							×	×								
Nevzorov							×	×								

Boatborne campaign. The oceanic component of CADDIWA aimed to measure optical, bio-optical, and biogeochemical parameters dedicated to the validation of routinely available lidar-derived oceanic products from the *Cloud–Aerosol Lidar and Infrared Pathfinder Satellite Observations* (*CALIPSO*) and the *Ice, Cloud, and Land Elevation Satellite 2* (*ICESat-2*) (e.g., Behrenfeld et al. 2013; Churnside et al. 2013; Lu et al. 2014; Dionisi et al. 2020; Liu et al. 2020), in order to fill an observational gap in the tropical ocean needed to validate these products. It also was designed to demonstrate the potential of *Aeolus* to derive subsurface ocean particulate backscattering parameter (b_{bp}) and the diffuse attenuation coefficient (K_d) in the UV, as well as assess *Aeolus* potential to derive biogeochemical parameters linked to ocean color and the ocean carbon cycle: colored dissolved organic matter, particulate organic carbon, and phytoplankton carbon. Finally, oceanic products derived from the airborne lidar LNG were also validated using boatborne observations acquired along the flight track of the Safire FA20 when it was operating near São Vincente.

Six 1-day outings at sea were performed south of the Sao Vicente Island between 9 and 22 September 2021 using the fishing boat "*Gamboa*." These ocean water sampling days at sea occurred during overpasses of *Aeolus* (9 coincidences on 10, 15, 17, and 22 September), *CALIPSO* (2 coincidences on 9 September), and *ICESat-2* (5 coincidences on 18 September). Oceanic measurements were also made along the Safire FA20 flight tracks on 10, 17, and 18 September (11 coincidences) in order to conduct comparison with LNG-derived oceanic products. Sixteen stations were established during the six outings to acquire several optical, bio-optical, and biogeochemical parameters (Table 1). A station in this context is a pause between two transits of the boat during which the submarine instrumentation is deployed. Reflectance R_{rs} just under the surface and diffuse attenuation coefficients in the water column were measured continuously between 350 and 900 nm using TriOS radiometers. The backscattering coefficient was measured using an ECO-volume scattering function meter from WetLabs at 532 nm and the absorption coefficient using an AC-S from WetLabs. Water samples were obtained using a Niskin bottle at different depths. The particulate organic carbon is here considered as particulate carbon from organic origin retained by a Whatman glass microfiber filter according to the Joint GlobalOcean Flux Study protocol (Knap et al. 1996). The particulate organic carbon is then composed of particles with a diameter between 0.4 and 200 μm, with prefiltration usually performed. The colored dissolved organic matter were obtained following de Matos Valerio et al. (2018).

Other CADDIWA assets. Additional notable CADDIWA assets included the following:

- A dedicated processing of IASI observations to retrieve the 3D distribution of the Saharan dust within the SAL over the ocean and in the vicinity of deep convection, based on the AEROIASI approach (Cuesta et al. 2020), for contextualization of airborne observations.
- A Global Navigation Satellite System (GNSS) station in Sal to monitor the evolution of total column water vapor (TCWV; Bock et al. 2021) alongside an AERONET sun photometer station to monitor aerosol optical depth (AOD).
- A contribution to the balloon radiosounding effort in Sal coordinated by the Karlsruhe Institute of Technology (KIT). Between 7 and 28 September, 38 GRAW balloons were launched from the airport, 9 of which corresponding to the time of *Aeolus* morning and/or evening overpasses.

CADDIWA Operations Center. All CADDIWA operations were coordinated from the CADDIWA Operation Center located in Hotel Morabeza in Santa Maria, Sal, close to the Amilcar Cabral

International Airport. The planning of CADDIWA airborne missions involved several steps, repeated daily during the deployment while the aircraft was operational (6–22 September 2021):

- Forecast teams' meetings were held at 0900 LT (1000 UTC) on a given day (hereafter denoted as *D*) to prepare the subsequent briefings using available material such as satellite imagery, weather predictions from national and international forecast centers, the cyclonic conditions monitored by the NHC, as well as dedicated aerosol Meso-NH and WRF-CHIMERE forecasts tailored for CADDIWA.
- Weather and atmospheric composition briefings took place at 1000 LT. A comprehensive analysis of the current situation was made in case of airborne operations scheduled on the day, as well as an assessment of the situation up to $D + 3$ in order to prepare upcoming airborne operations.
- CADDIWA mission proposal meetings were held at 1100 LT to discuss the Safire FA20 aircraft operation proposals for the following 3 days ($D + 1$, $D + 2$, and $D + 3$).
- JATAC coordination meetings with DLR (physically) and other JATAC participants (remotely) at 1200 LT under the guidance of ESA.
- Weather and atmospheric composition update briefings took place at 1900 LT, during which the evolution of the situation was monitored, and the impact on the flight planning was assessed.

More details on the CADDIWA team can be found in the supplementary material.

On days when the Safire FA20 flew, preflight briefings and flights debriefings were held directly at the airport. During airborne operations, the CADDIWA Operation Center monitored the weather situation and updated the mission scientists as needed through the chat capability of the PLANET communication system from the ATMOSPHERE company.

Daily operation reports were compiled at the end of each day, which summarized the major weather and atmospheric composition information for the record, as well as an outline of the CADDIWA flight conduct, an update on the instruments status and operations by other JATAC teams.

Regional aerosol simulations were carried out using two state-of-the-art French national "codes communautaires," namely, WRF-CHIMERE (Menut et al. 2021) and Meso-NH (Lac et al. 2018). CHIMERE is a chemistry transport model forced by meteorological fields from WRF. The models include newly developed aerosol–cloud interaction parameterization (Meso-NH; Hoarau et al. 2018a,b; CHIMERE; Tuccella et al. 2019), in order to quantify the aerosol–radiation–cloud interactions (i.e., all three effects mentioned above) accounting for the spatial and temporal variability of remote aerosol sources over the Sahara and the Sahel, and assess the aerosol radiative effects at the regional scale. Operational forecasting chains were designed and tested starting in July 2021 in order for the forecasts to be available during September 2021 to assist in the planning of airborne operations. Both models have a strong record of efficacious contribution to previous projects on the topic. The "operational" forecasting chain for Meso-NH has already been successfully implemented in campaigns such as FENNEC (Chaboureau et al. 2016) and AEROCO-sA (Formenti et al. 2019). Concerning WRF-CHIMERE, the operational chain is used daily in numerous air quality networks, for the French PREVAIR system and the European Centre for Medium-Range Weather Forecasts (ECMWF) Copernicus Atmospheric Monitoring Service (CAMS) forecast.

The WRF-CHIMERE operational chain was initialized with National Centers for Environmental Prediction (NCEP) forecast of the previous day ($D - 1$) at 1800 UTC, which is made available at 0000 UTC on the day of interest (current day, *D*). The CHIMERE forecasts were available to the CADDIWA forecasting team around 0400 UTC (0300 LT in Sal) for the period

covering D to D + 4. CHIMERE simulations consisted of two nested domains, one domain with a resolution of 60 km, covering a large area including Sahara and Sahel, and one domain with a resolution of 4 km (10°–24°N, 30°–15°W), centered on Sal. The CADDIWA operational chain is described in Menut (2023).

Meso-NH simulations also consisted of two nested domains with a resolution of 4 and 16 km, the larger domain covering the Sahara and the Sahel, and the smaller one being the same as the inner domain of the WRF-CHIMERE simulations. Two sets of forecasts were made: 3-day forecasts with the two domains (referred to as EP) and 5-day forecasts on the larger domain (referred to as EA). EP simulations used 1200 UTC ECMWF analyses at D-1 as initial fields and were available at 0900 LT every day. EA simulations started from ECMWF analyses at 0000 UTC on D and were available at 1400 LT every day, for the CADDIWA evening briefings. The vertical grid was made of 32 levels and the vertical mesh increased from 100 m near the surface to 1 km at the top of the model. Simulations were run with the Kain–Frisch shallow convection scheme (Pergaud et al. 2009), the one-moment bulk microphysics scheme of Pinty and Jabouille (1998), the Dust Entrainment and Deposition (DEAD) scheme (Zender et al. 2003), a Lagrangian online back trajectories capability and the capacity to produce synthetic satellite images thanks to the use of the Rapid Radiative Transfer Model (Mlawer et al. 1997). Additional details on the dedicated CADDIWA forecasts products can be found in the supplemental material.

Summary of major accomplishments and science highlights

This section provides first highlights of notable events and unique opportunities for research enabled by the field campaign, including an overview of tropical cyclones forming in the eastern tropical North Atlantic in September 2021, cases of developing and nondeveloping AEWs, RALI-derived wind measurements and comparison with *Aeolus* and bio-optical measurements in the Cape Verde waters.

Overview of tropical cyclones forming over the eastern North Atlantic in September 2021. The year 2021 was the third most active year on record in terms of named storms according to the NHC, 21 in all, marking the sixth consecutive above-normal Atlantic hurricane season.

Category 3 Hurricane Larry (30 August–11 September) had already formed over the tropical North Atlantic when the CADDIWA Operational Center began operation on 6 September. Larry originated from a strong tropical wave that emerged off the west coast of Africa on 30 August. By 1800 UTC 31 August, the convective organization increased enough for the system to be designated as a tropical depression when it was located about 280 n mi south-southeast of the Cape Verde Islands. The signature of the atmospheric moisture associated with Larry is also apparent in the GNSS-derived TCWV time series collected in Sal (Fig. 2).

The first notable weather feature that came across Sal during the CADDIWA detachment occurred on 11 September (see its temporal evolution in Figs. 3a–f). It was associated with an intense AEW moving out of West Africa from Guinea, south of Senegal, on 10 September (Fig. 3c). The NHC started to follow that feature and provided best track estimates of it over the continent (Guinea and Mali) starting at 0000 UTC on that day and continuing through 2300 UTC 12 September (Fig. 3e). However, the wave did not develop into a TS, and hence was not given a number or a name by the NHC. In this paper, we shall refer to it as a TP, and we have decided to tag it as "Pierre Henri," in memoriam of the late Pierre Henri Flamant.[1] As it passed over Sal (Fig. 3d), the signature of Pierre Henri was evident on the GNSS-derived TCWV series (Fig. 2) and was associated with the

[1] Pierre H. Flamant is one of the founding fathers of lidar technology for atmospheric observation, with an expertise widely recognized throughout the world. The pioneering work of Pierre H. Flamant still guides a large part of the lidar community observational activities, whether it be the development of instruments or satellite missions (www.insu.cnrs.fr/en/node/4197).

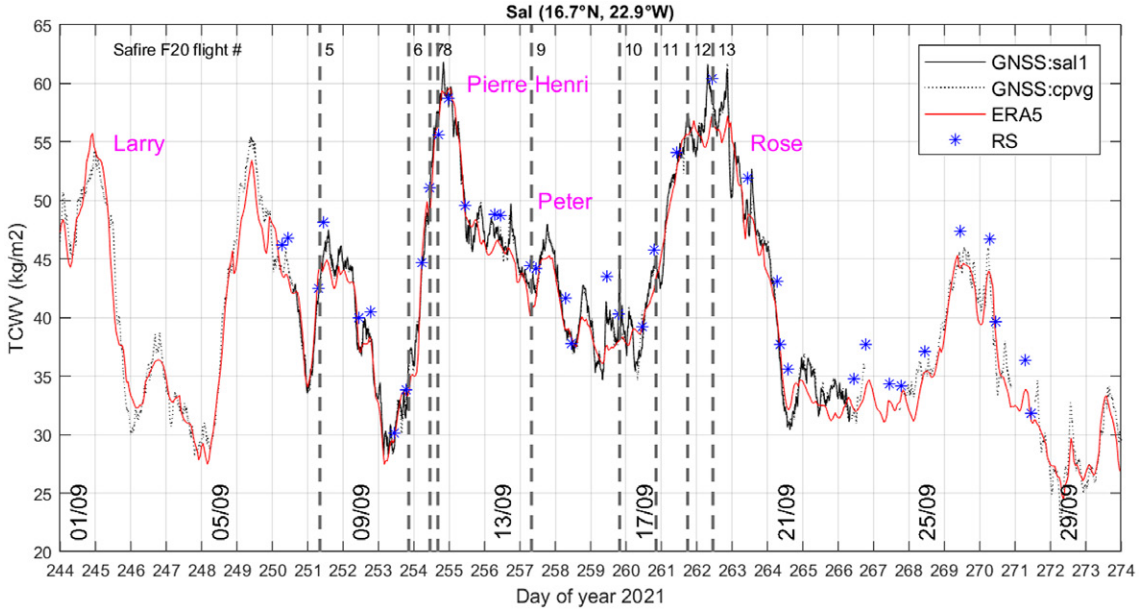

Fig. 2. TCWV time series for September 2021 at Sal as observed from two GNSS stations: CPVG (green dashed line) the permanent station operated by INMG and IGN, and SAL1 (black solid line), the collocated temporary station installed for the CADDIWA campaign, as well as the fifth ECMWF reanalysis (ERA5) (red solid line) and radiosondes launched from Sal (blue asterisks). Black dashed vertical lines indicate the midflight times of the Safire FA20 operations on 8 (flight F5), 10 (F6), 11 (F7 and F8), 14 (F9), 16 (F10), 17 (F11), 18 (F12), and 19 (F13) September 2021 (see Table 2). The time at which the environments of TS Peter and Rose were probed in Sal is also indicated.

highest values observed during the CADDIWA detachment period. Two Safire FA20 flights were dedicated to the documentation of the environment of TP Pierre Henri.

The life cycles of the short-lived TSs Peter and Rose were quite similar over the Atlantic Ocean and occurred during the same period, i.e., 19–22 September, but farther west in the case of TS Peter. Both started as disturbances over the continent on 12 September (Fig. 3e), which moved from West Africa over the Atlantic on 14 and 16 September (Figs. 3g,i) for Peter and Rose, respectively, producing large bursts of convection but lacking a closed circulation. In both cases, convection became more concentrated as the features moved westward, and both systems acquired a closed circulation on 19 September. As a result, tropical disturbances developed by 0000 UTC 19 September with the first signs of the formation of Peter occurring about 540 n mi east of the French Antilles and those of Rose occurring around 335 n mi south-southwest of the Cape Verde Islands. The depression intensified into TS Peter at 0600 UTC on the same day, whereas the transition to TS Rose occurred near the end of the day on 19 September. The signature of the atmospheric moisture associated with TS Rose is apparent in the GNSS-derived TCWV time series (Fig. 2), unlike for TS Peter, which can hardly be detected. The lack of the moisture peak for Peter because of the fact that the disturbance was too far south of Sal, putting Sal more in the dry air of the Saharan air layer. Two Safire FA20 flights were dedicated to the documentation of the environment of the TS Rose, on 18 and 19 September. The pre-TS Peter environment was deemed too far south of Sal to trigger dedicated Safire FA20 operations.

Unlike Larry, the signature of category 4 Hurricane Sam (22 September–5 October) cannot be seen in the TCWV time series in Sal (Fig. 2) as it formed and traveled westward over the Atlantic too far to the south from Cape Verde. Sam stemmed from a combination of tropical waves (namely, an AEW, a mixed Rossby–gravity wave, and an equatorial Rossby wave) that moved off the west coast of Africa and into the Atlantic on 19 September, while operations at the CADDIWA Operational Center were still underway. The wave was associated with convective activity as it moved westward to the south of the Cape Verde Islands on the

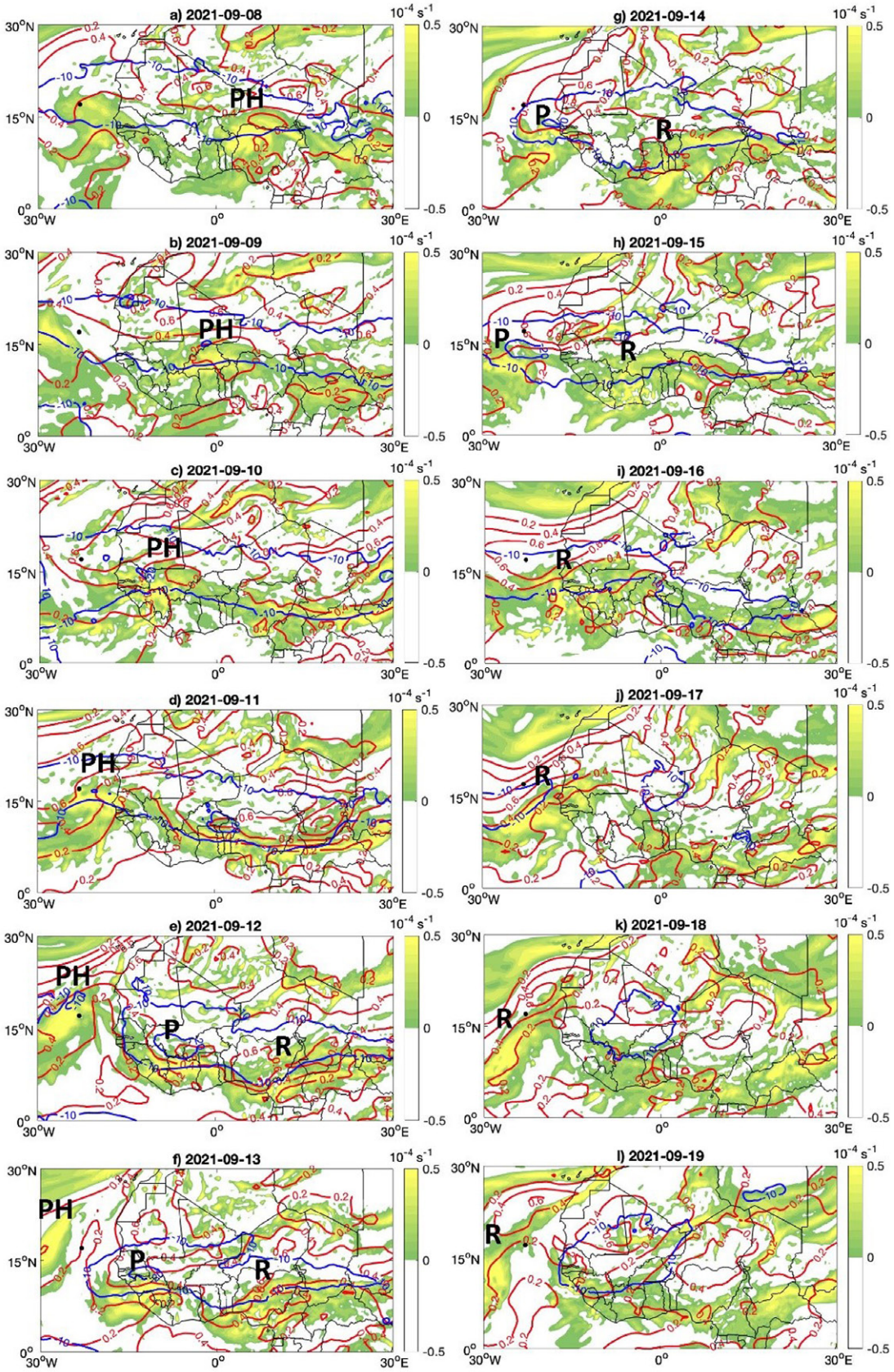

Fig. 3. Daily evolution of the atmospheric dynamics and aerosol content from (a) 8 to (l) 19 Sep 2021 over West Africa and the tropical North Atlantic. Shading represents the relative vorticity at 700 hPa; only positive values are displayed to highlight cyclonic circulations favorable to convection. Blue contours represent the zonal wind at 600 hPa (m s^{-1}); only negative values are displayed to highlight the AEJ location. Red contours represent the aerosol optical depth at 550 nm. Relative vorticity and zonal wind data are extracted from the ERA5 product; aerosol optical depth data are extracted from the CAMS reanalysis product. The black dot at 17°N, 23°W indicates the coordinates of Cape Verde. The perturbations leading to the development of Pierre Henri, Peter, and Rose are labeled as PH, P, and R, respectively.

following day. By 1800 UTC 22 September, it became a tropical depression approximately 590 n mi west-southwest of Cabo Verde's southernmost islands. The depression intensified into TS Sam around 0600 UTC September 23. Late on 25 September, it became a category 4 hurricane.

Nondeveloping AEW—Tropical Perturbation Pierre Henri. On 11 September 2021, 2 Safire FA20 flights were conducted in the environment of the approaching TP Pierre Henri. The associated AEW was first detected over the continent on 8 September (Fig. 3a) and the AEW trough predicted to deepen upon reaching Dakar on 11 September (Fig. 3d). The TP had an unusual northwestward path over Sal on that day and was moving into a thick widespread dust plume associated with the SAL. According to Jonville et al. (2023, manuscript submitted to *Quart. J. Roy. Meteor. Soc.*), Pierre Henri benefited from a supply of low-level vorticity over the continent that led to the development of a coherent vorticity column before reaching the Atlantic. This vertical structure favored convective systems over the continent, where no significant humidity flux could balance the loss of water content due to convective precipitation, thereby leading to a drying of the air inside the cyclonic circulation. In addition, due to its northern location, the cyclonic circulation associated with Pierre Henri also incorporated air from the SAL over the ocean, which also contributed to the drying of the air. Those two processes prevented the development of Pierre Henri into a TS.

The large dust outbreak was captured by AEROIASI in the morning of 10 September, over the Cape Verde Islands (Figs. 4a–c). Dust was transported from North Africa (Morocco, Mauritania, Algeria), just north of Pierre Henri which was located near the coast of West Africa. The mean altitude of the dust plume over Sal was almost 5 km MSL (Fig. 4b), with dust being observed as high as 6 km MSL (Fig. 4c). On the next day, in the morning, the dust plume was observed to swirl around the center of Pierre Henri mostly to the north and west of the Cape Verde Islands (Figs. 4d,e). According to AEROIASI, the core of the dust plume was between 3 and 5 km MSL (mean layer height at 4 km MSL), and it was thickest west of Cape Verde (about 5–6 km).

The dry air and dust circling ahead of the approaching TP, as well as the anvil of the approaching storm was documented during the morning Safire FA20 track. Figure 5a shows the dust RGB composite from the Spinning Enhanced Visible and Infrared Imager (SEVIRI) on board Meteosat Second Generation at 1100 UTC 11 September, with the flight track and the position of the released dropsondes overlain.

During the morning flight, the dry and dust-laden SAL was first sampled in situ at ~3.6 km MSL as the Safire FA20 was flying away from the storm (from 0916 to 0947 UTC) and then remotely along the same track, but from a higher altitude (~9.3 km MSL), as the aircraft was flying toward the TP (between 1006 and 1115 UTC, Fig. 6). Figures 6a and 6b display the LNG backscatter at 532 nm and depolarization ratio at 355 nm, respectively, acquired along the flight, and shows the location of the five dropsondes that allowed retrieving complete dynamical and thermodynamical profiles between 0 and 8 km MSL. The deep convection associated with TP Pierre Henri (evidenced by the high backscatter values at the altitude of the aircraft in Fig. 6a) was then sampled in situ at different levels (~9.3 and 4.2 km MSL) between 1115 and 1230 UTC. Figure 6c shows a cross section of dust extinction, cloud water content, and potential temperature forecasted by Meso-NH along the Safire FA20 flight track between 0900 and 1300 UTC. In the part of the flight that is free of midlevel clouds, the structure of the dust layer is consistent with the LNG observations. The forecast suggests that the dust layer is also present underneath the midlevel clouds and even, to a much lesser extent, under the cloud anvil associated with Pierre Henri.

The widespread dust layer seen in Fig. 4d was sampled in situ and with LNG in the first stages of the flight (Fig. 6). The dust layer extended from 1 to 5 km MSL, above the marine

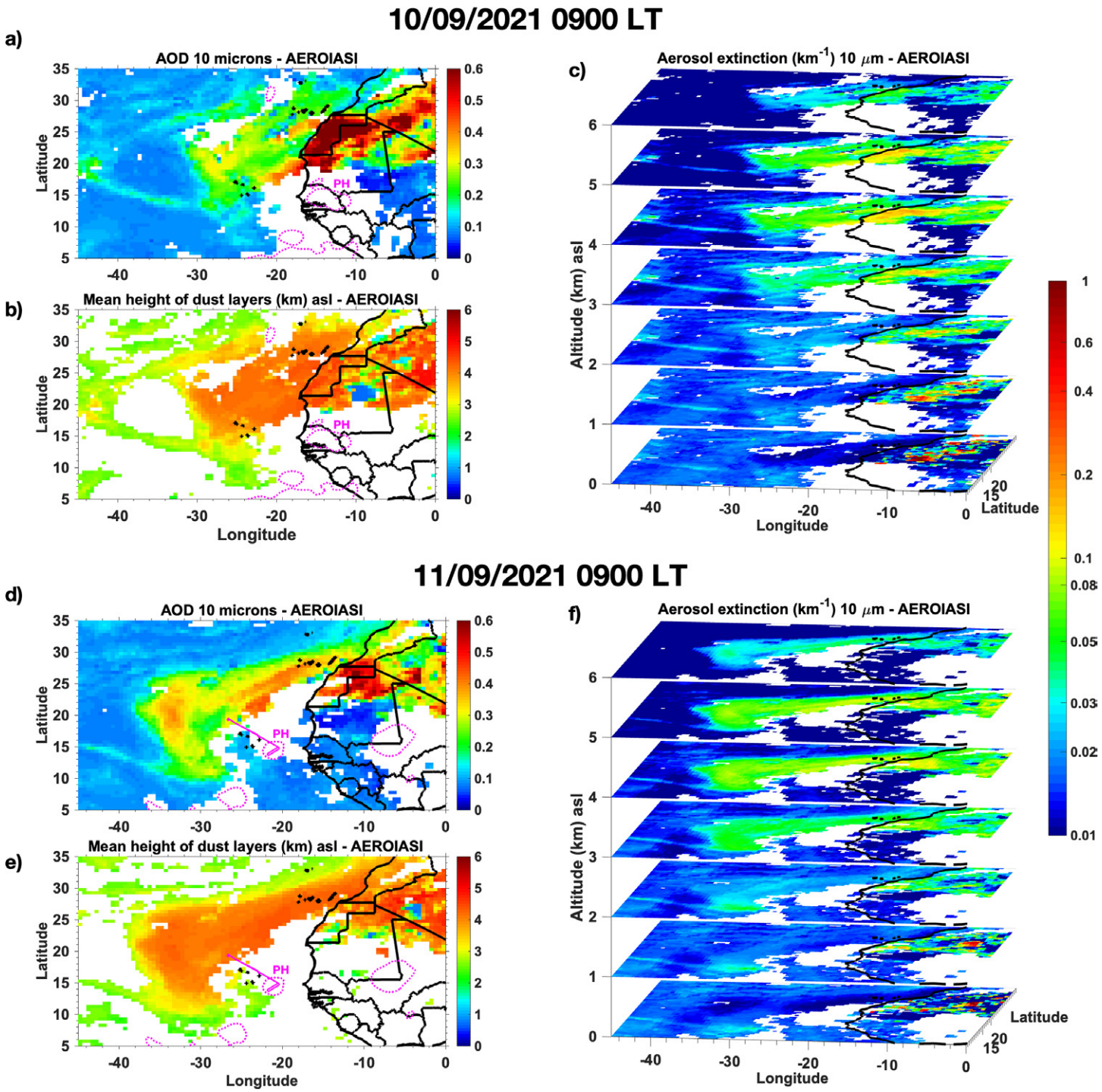

Fig. 4. AEROIASI-derived (a) dust AOD at 10 μm, (b) mean layer height, and (c) 3D dust distribution in the morning of 10 Sep 2021. These AEROIASI products are based on the IASI observations made from three platforms (*MetOp-A*, *MetOp-B*, and *MetOp-C*) merged together, the equatorial crossing time of which are separated by less than 1 h, around 0900 LT Cape Verde (1000 UTC). Areas in white in the plots indicate the presence of clouds that prevent AEROIASI retrievals. The mean aerosol layer height is estimated as the height below which the AOD is half that of the total column. (d)–(f) As in (a)–(c), respectively, but for 11 Sep in the morning. The magenta line in (d) and (e) is the Safire FA20 flight track. The dotted magenta contours represent brightness temperature isotherm 245 K indicative of the most active convective clouds associated with PH. The color bar of the 3D plots in (c) and (f) is the one located on the rightmost part of the figure.

boundary layer (the top of the marine boundary layer being marked by the presence of low-level cumulus clouds). The dust layer is clearly seen until 1045 UTC and its dynamical and thermodynamical environment depicted by the first dropsonde released at 1021 UTC (DS1, Fig. 5b, red filled circles). After 1045 UTC, the Safire FA20 overflew a midlevel cloud deck that prevented unambiguous retrievals with LNG. However, the model suggests that

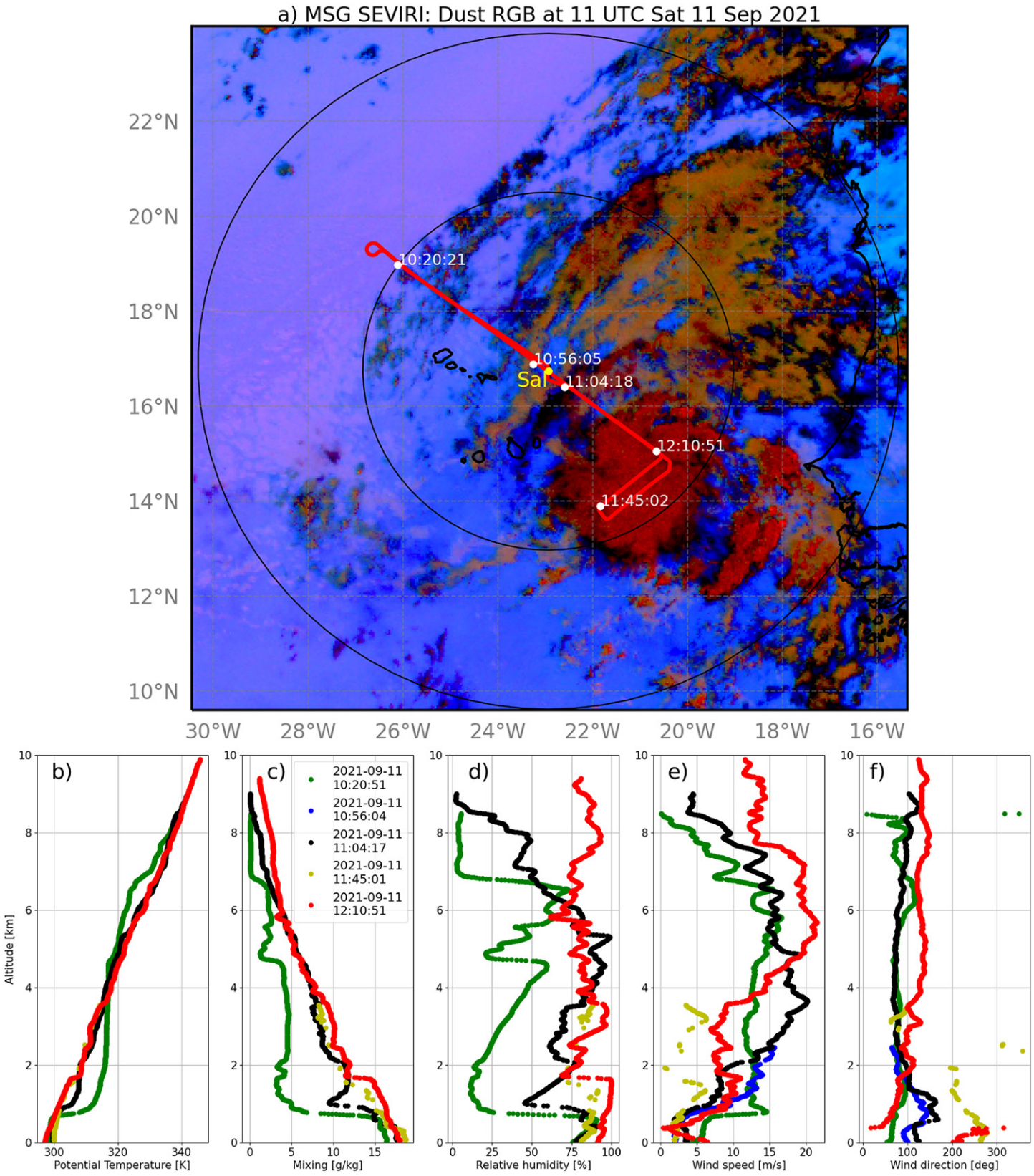

Fig. 5. (a) Safire FA20 flight track (red) overlain on the Spinning Enhanced Visible and Infrared Imager (SEVIRI) dust RGB composite at 1100 UTC 11 Sep. Pink indicates the presence of dust while dark red indicates high-level clouds. The location of the dropsonde releases are also shown as white dots. The Cape Verde Islands are highlighted by thick black lines. The two black circles indicate the distance from Sal, the outer one being at 425 n mi and the inner one at 225 n mi. (bottom) Profiles of (b) potential temperature, (c) water vapor mixing ratio, (d) relative humidity, (e) wind speed, and (f) wind direction, obtained from the five dropsondes released from the Safire FA20 in the morning of 11 Sep 2021 (DS1 in green, DS2 in light blue, DS3 in yellow, DS4 in gray, and DS5 in dark blue).

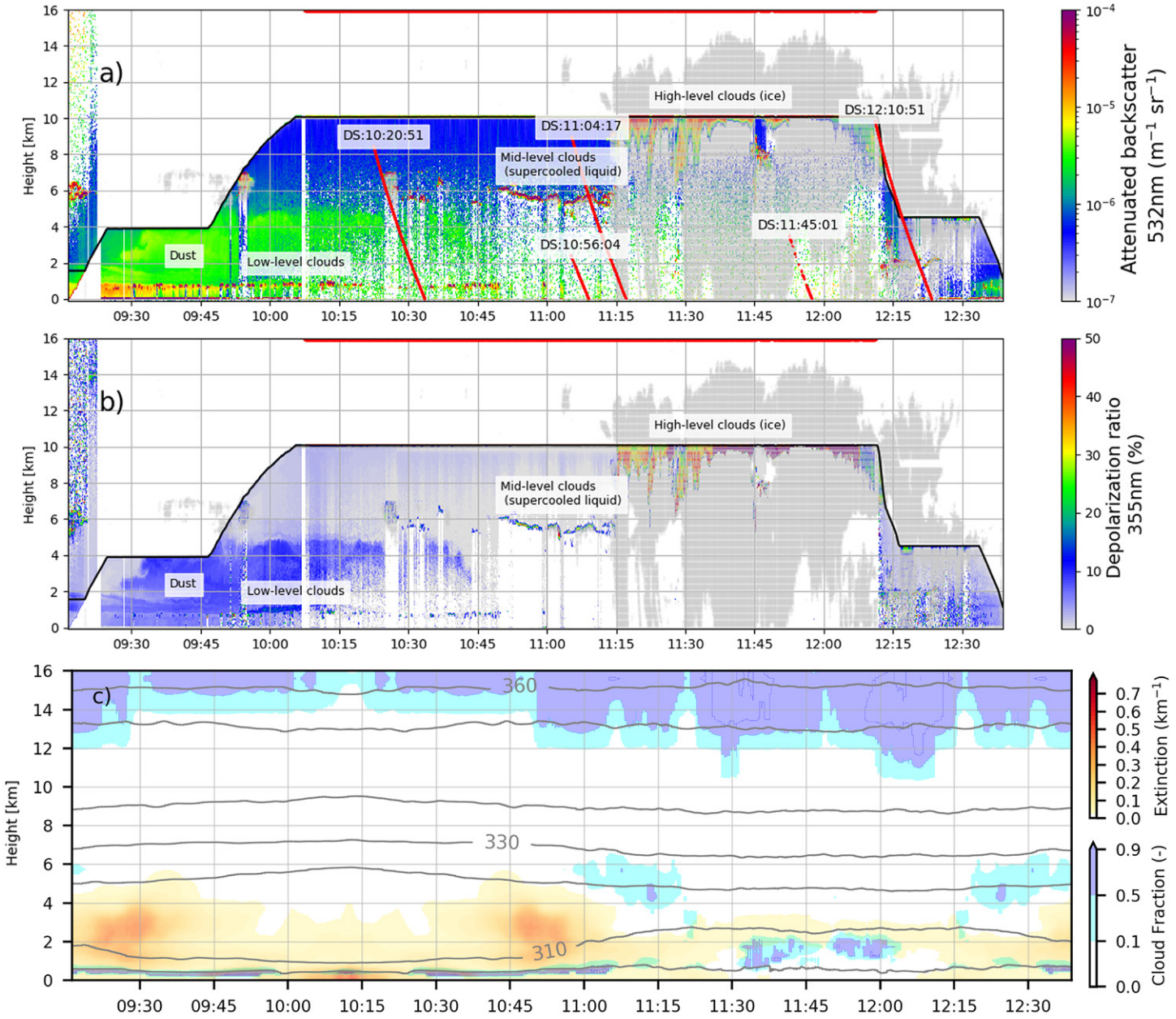

Fig. 6. LNG-derived (a) backscatter signal at 532 nm and (b) depolarization ratio during the Safire FA20 flight 7 on 11 Sep 2021. Radar reflectivity is overlain in light gray. The reddish colors in (a) indicate clouds while the dust layer sampled at the beginning of the flight (between 0900 and 1045 UTC) between 1 and 5 km MSL appears in green in (a) and blue in (b). (c) Vertical cross section of dust extinction (warm colors), cloud water content (cold colors), and potential temperature along the Safire FA20 flight track extracted from the Meso-NH 4-km domain between 0900 and 1300 UTC.

the dust extends into later times (Fig. 6c). The dynamical and thermodynamical environments associated with the portion of flight above the midlevel clouds were well captured by dropsondes at 1056 and 1104 UTC (DS2 and DS3, Fig. 5b). Finally, two dropsondes were released in the deep convective region associated with Pierre Henri (DS4 and DS5, at 1145 and 1210 UTC, respectively, Fig. 5b).

The SAL west of TP Pierre Henri consists of a deep adiabatic layer between 1 and 5 km MSL (see potential temperature profile from DS1 in Fig. 5b) advected from the northeast (Fig. 5f), characterized by a water vapor mixing ratio of ~5 g kg^{-1} (Fig. 5c) and increasing relative humidity from the bottom to the top of the layer (Fig. 5d). Another adiabatic layer, characterized by a water vapor mixing ratio of ~3 g kg^{-1} (Fig. 5c), advected from the southeast (Fig. 5f), is present between 5 and 7 km MSL which is also exhibiting increasing RH with height, allowing clouds to form atop (as evidenced by lidar measurements around 1055 UTC in Fig. 6a).

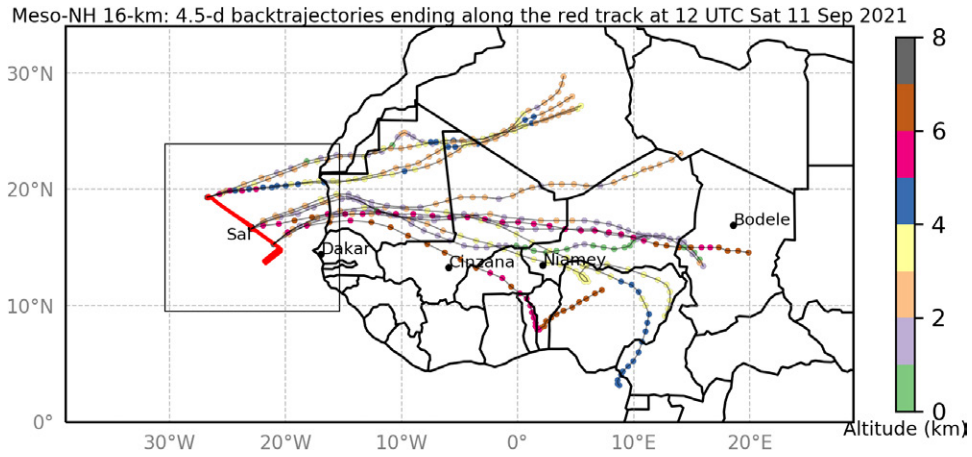

Fig. 7. Meso-NH simulation on the 16-km-resolution domain showing 4.5-day back trajectories ending at 1200 UTC and ending at 2.4, 2.7, 3.2, and 5.7 km MSL along the Safire FA20 flight track shown in Fig. 6c. Dots represent the evolution of the back trajectories every 3 h.

The subsequent dropsondes released as the aircraft was approaching the storm evidenced the moistening of the lower troposphere. Measurements made within the cloud anvil evidence the moist environment associated with Pierre Henri, with relative humidity above 70% from 0 to 9 km MSL, and nearly saturated conditions below 1.75 km MSL (DS5 in Fig. 5b). Strong winds between 4 and 8 km MSL, peaking above 20 m s^{-1}, and coming from the southeast were also observed, likely associated with an undulating AEJ (Fig. 3d). The depth of the marine boundary layer was also observed to decrease with the distance from the center of TP, from 1.8 to 1 km, with low-level winds veering from southerly to easterly, consistent with low-level air masses swirling around the Pierre Henri (Fig. 5b).

Figure 7 shows the Meso-NH 16-km domain with 4.5-day back trajectories ending at 1200 UTC at 3,000 m MSL on 11 September, along the Safire FA20 track shown in Fig. 6c. The origin of the dust outbreak to the northwest of the flight track is northern Africa, while the dust sampled by LNG in the middle and southern parts of the flight is from Sahel, and potentially originating from the Bodélé depression, known to be the most prominent dust emission source in West Africa (Washington and Todd 2005). The processes associated with this differential dust transport will also be further investigated.

Into the environment of TS Rose precursor. In this section we want to highlight the variety of observations obtained during the campaign and the synergies between these different pieces of information toward a better comprehension of aerosol–cloud–dynamics interactions in the environment of developing TS.

According to Jonville et al. (2023, manuscript submitted to *Quart. J. Roy. Meteor. Soc.*), the developing AEW, which ultimately was associated with TS Rose, benefited from a low-level positive vorticity supply over the ocean in the monsoon trough region. Furthermore, the intensifying cyclonic circulation did not incorporate air from the SAL as it was too far south. The resulting closed circulation created a protective pouch in which deep convection developed while being sheltered from any intrusion of dry air (Dunkerton et al. 2009), allowing the transition from a tropical depression to a TS.

The cloud, aerosol, and dynamical environments associated with soon-to-become TS Rose (Figs. 3j–l) near Cape Verde at 1000 UTC 19 September 2021 is shown in Fig. 8. The flight plan was designed to reach the center of the depression and release a dropsonde there. According to the Meso-NH forecast, the Safire FA20 did reach the center of the low (~1,009 hPa), which is also evidenced by the strong circling winds at 10 m MSL (Fig. 8d). The 10-m winds show a circulation consistent with the area of low pressure. At 4 km, the circulation is displaced

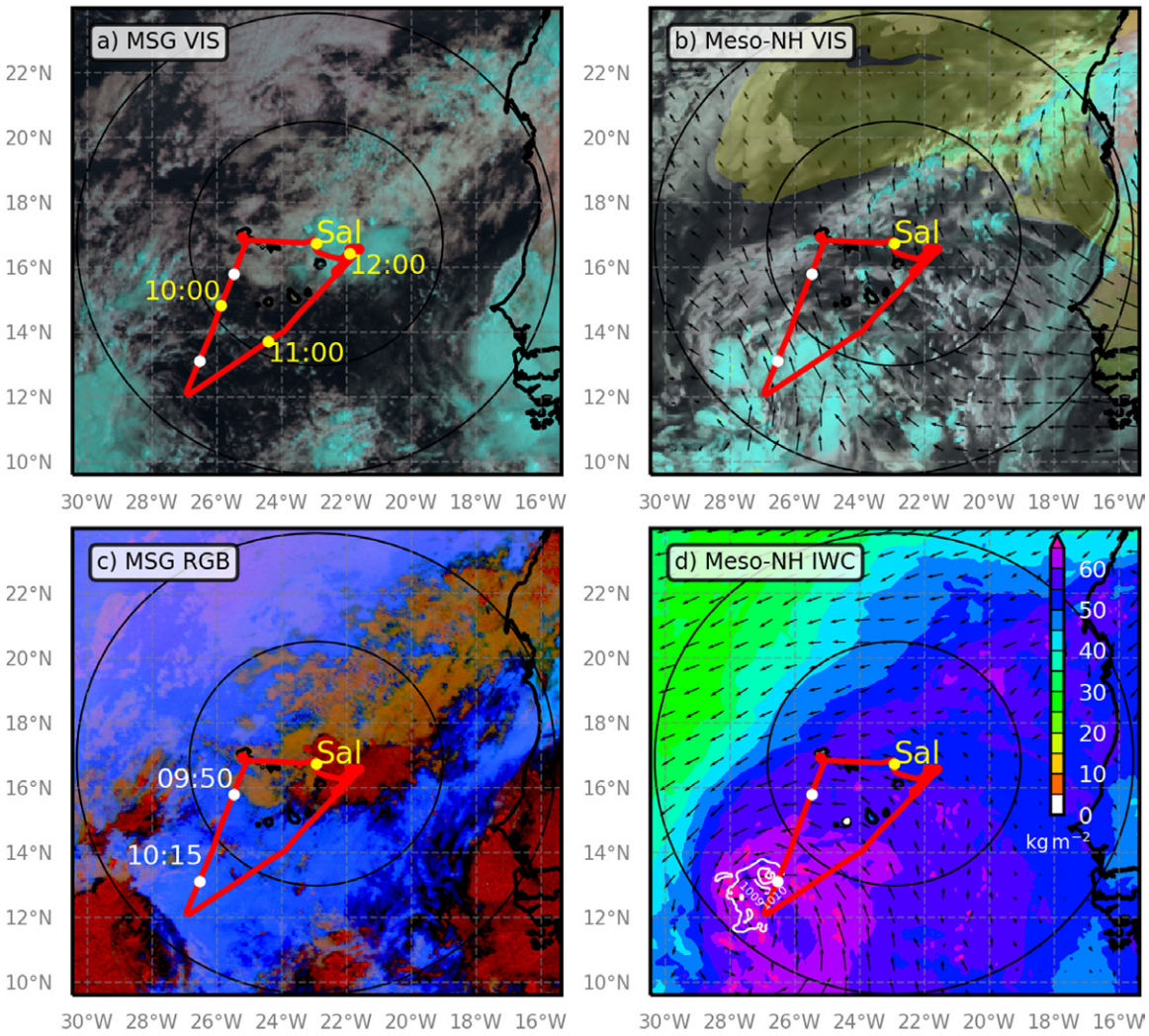

Fig. 8. Weather situation at 1000 UTC 19 Sep 2021 associated with the tropical disturbance that will become TS Rose later on that day. (a) MSG reflectance in the visible. (b) Synthetic reflectance in the visible from the Meso-NH model forecast and aerosol optical thickness (>0.1) in brown. Winds at 4-km altitude are also indicated (arrows). (c) RGB MSG image showing high clouds (red), midlevel clouds (dark brown), and low clouds (light brown), as well as terrigenous aerosols (pink). (d) TCWV in color, sea level pressure (white contours) and wind at 10 m (arrows). The Safire FA20 flight track is shown in red throughout the panels, the white dots locate the sondes dropped from the aircraft, and the black dot indicates the airport at Sal.

significantly to the southwest (Fig. 8b), indicating a sheared, non–vertically aligned system. The TCWV simulated with Meso-NH was also largest in the vicinity of the closed low pressure circulation (in excess of 60 kg m^{-2}, Fig. 8d), while it was only between 50 and 60 kg m^{-2} near Sal, consistently with GNSS-derived TCWV (Fig. 2). There is a sharp southeast–northwest gradient of TCWV according to Meso-NH, with a much drier atmosphere in the convection-free areas to the northwest of Cape Verde as shown in the SEVIRI infrared imagery (Fig. 8c). Thanks to SEVIRI, there is evidence of the presence of dust in this area (Fig. 8c), as also suggested by the Meso-NH simulation (Fig. 8b). SEVIRI imagery in the visible and infrared (Figs. 8a,b) evidence the nearly cloud-free conditions along most of the flight track, while the deep convection associated with the closed circulation of TS Rose being located to the southwest of the southernmost way point of the track, likely due to the sheared environment. This is corroborated by the RASTA cloud radar reflectivities (Fig. 9a). There appears to be quite a difference in the representation of clouds in the model versus the satellite imagery with deep clouds in the model appearing to be organized near the center of circulation.

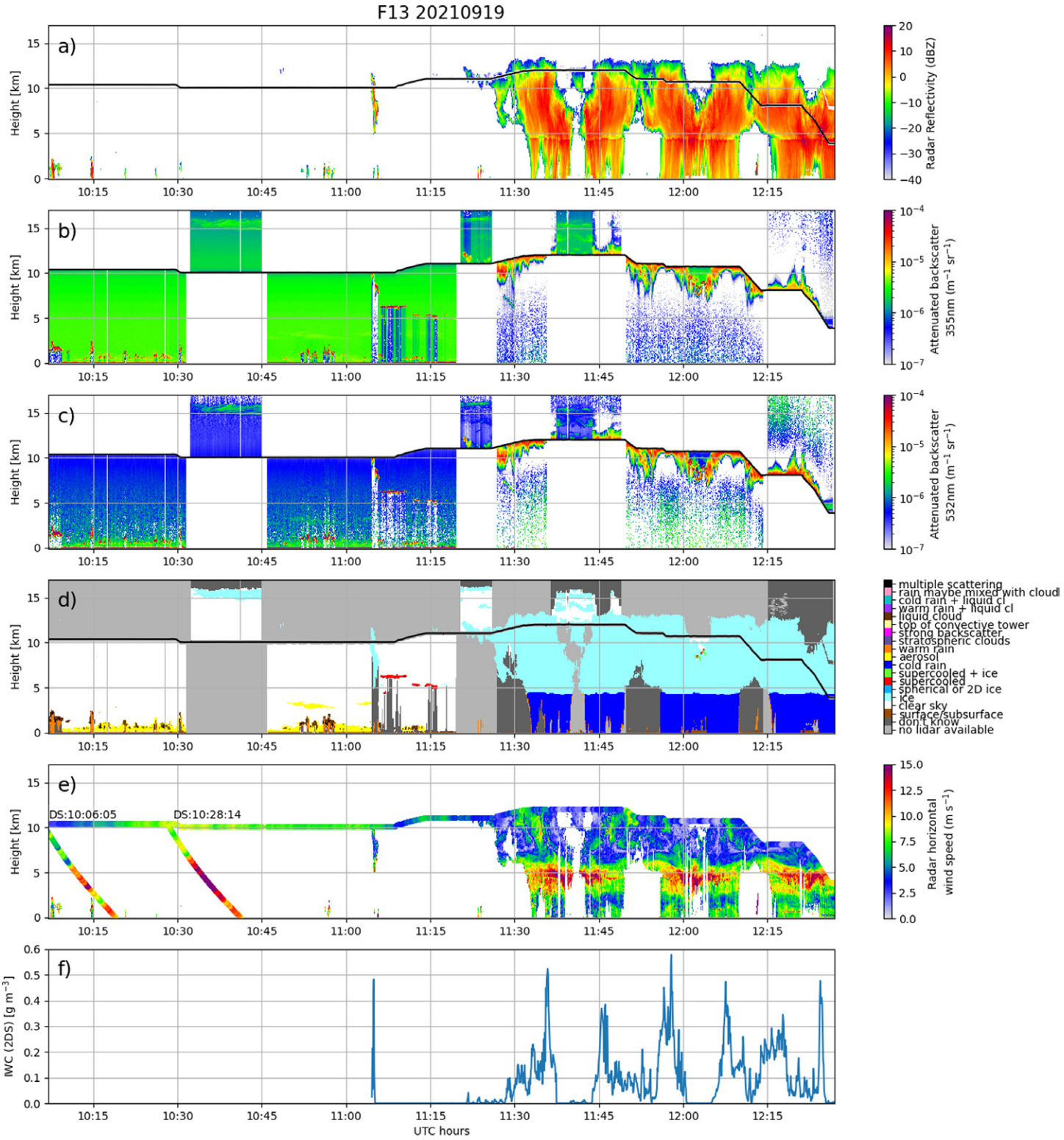

Fig. 9. Measurements collected from the Safire FA20 during flight 13 on 19 Sep 2021: (a) Radar reflectivity (nadir and zenith antennas) measured by the RASTA Doppler cloud radar; the black line indicates the altitude of the aircraft. (b),(c) Lidar calibrated attenuated backscatter at 355 and 532 nm, respectively (pointing alternatively between nadir and zenith). (d) The radar–lidar target categorization is presented, showing the complementarity of the two instruments, i.e., the high sensitivity of the lidar and the penetration capability of the radar. Ice appears in light blue, rain in dark blue, supercooled layers are depicted in red, and aerosols appear in yellow. Light gray indicates areas where there is no lidar information and dark gray corresponds to the areas where the lidar beam is extinct due to the presence of optical thick liquid water clouds (and hence the entire depth of the cloud cannot be probed). The combination of the three downward antennas using the Doppler radar allows one to retrieve the horizontal wind speed of both cloud and precipitation particles [(e) aircraft wind measurements are show at the altitude of the aircraft]. (f) The ice water content derived from the 2DS probe, and assuming a Baker and Lawson (2006) mass–size relationship, is depicted.

On 19 September, the environment of deep convection was sampled with the Safire FA20, but close to Sal, not near the closed circulation to the south. Deep convection near Sal reached almost 13 km MSL (Fig. 9), and was sampled in situ (microphysics probes) and remotely (radar) at seven levels from 4 km (cloud base) to 11.1 km, allowing to document the properties of liquid and frozen hydrometeors up to −50°C. The capability of the radar–lidar combination to derive multiple variables of interest for the analysis of aerosol–cloud–dynamics interactions is illustrated in Fig. 9, along with in situ cloud microphysics observations of the ice water content derived from the 2DS probe. The LNG observations in the first part of the flight (1015–1115 UTC) confirm that the atmosphere was nearly cloud- and dust-free. Cirrus clouds were observed above 15 km MSL. In the region of deep convection near Sal, the radar–lidar target categorization evidences that the isotherm 0°C (melting layer, transition from light to darker blue, Fig. 9d) was at 4.5 km MSL, consistently with the dropsonde temperature measurement (not shown). Horizontal winds derived from RASTA highlight strong winds (in excess of 13 m s^{-1}) just below 4 km, as well as in the marine boundary layer, below 2 km MSL. The altitudes and strengths of these jets are consistent with dropsonde measurement made to the west of the area.

Anticipated research toward aerosol–cloud–dynamics interactions will deal with the impact of the dust load on the development of AEWs and other tropical waves over the Atlantic Ocean, as well as the impact of the structure, growth, and propagation of the tropical waves on the zonal dust transport. Other anticipated research will focus on establishing which of the three dust effects dominates/controls the intensification of MCS mesovortices offshore and eventually their transition to TSs over the Atlantic Ocean.

Aeolus *wind verification.* Five dedicated Safire FA20 flights were made during the campaign along *Aeolus* orbits with the objective to document aerosol and wind gradients and to collect sufficient wind and aerosol data to intercompare with a significant number of L2A (aerosol) and L2B (wind) *Aeolus* products profiles (nominal horizontal resolution of 87 km). *Aeolus* provides horizontal line-of-sight (HLOS) wind observations in aerosol-laden (referred to as Rayleigh-clear winds) and cloudy atmospheres (so-called Mie-cloudy winds). The length of the Safire FA20 legs above and in the dust layer was set to be at least 240 n mi (450 km) in order to allow meaningful comparisons with at least five *Aeolus* L2B profiles. LNG measurements along the upper leg were performed in the so-called *Aeolus* mode, i.e., pointing 37° sideways, while they were made in nadir pointing mode along the lower leg. Dedicated Safire FA20 *Aeolus* flights were made in a variety of AOD conditions: flight F5 occurred in low AOD conditions, with AOD less than 0.4, while flight F6 took place in high AOD conditions (AOD ~ 1). Flights F9, F10, and F11 were conducted under moderate AOD conditions ranging from ~0.55 for F9 to ~0.65 for flights F10 and F11.

Thanks to its Doppler capability at 355 nm, LNG allows retrieving the HLOS velocity of aerosol and cloud particles that can be compared to *Aeolus* L2B products, provided that a correction is applied to the LNG data to account for the difference in observation geometry between *Aeolus* and LNG (e.g., Lux et al. 2020). A similar approach can be applied in order to compare *Aeolus* products and dropsonde-derived winds projected along the *Aeolus* HLOS (e.g., Martin et al. 2021).

Figure 10 shows the LNG-derived particulate signal at 355 nm during flight F11, as well as the LNG-derived HLOS velocity. During this flight, a complex layering of dust was observed in the southern part of the flight track along the *Aeolus* orbit, between 2 and almost 6 km MSL. The depth of the marine boundary layer was also observed to increase between the southern and the northern part of the leg (between 1900 and 2030 UTC). Cumulus clouds were observed at the top of the marine boundary layer as well as near the top of the dust

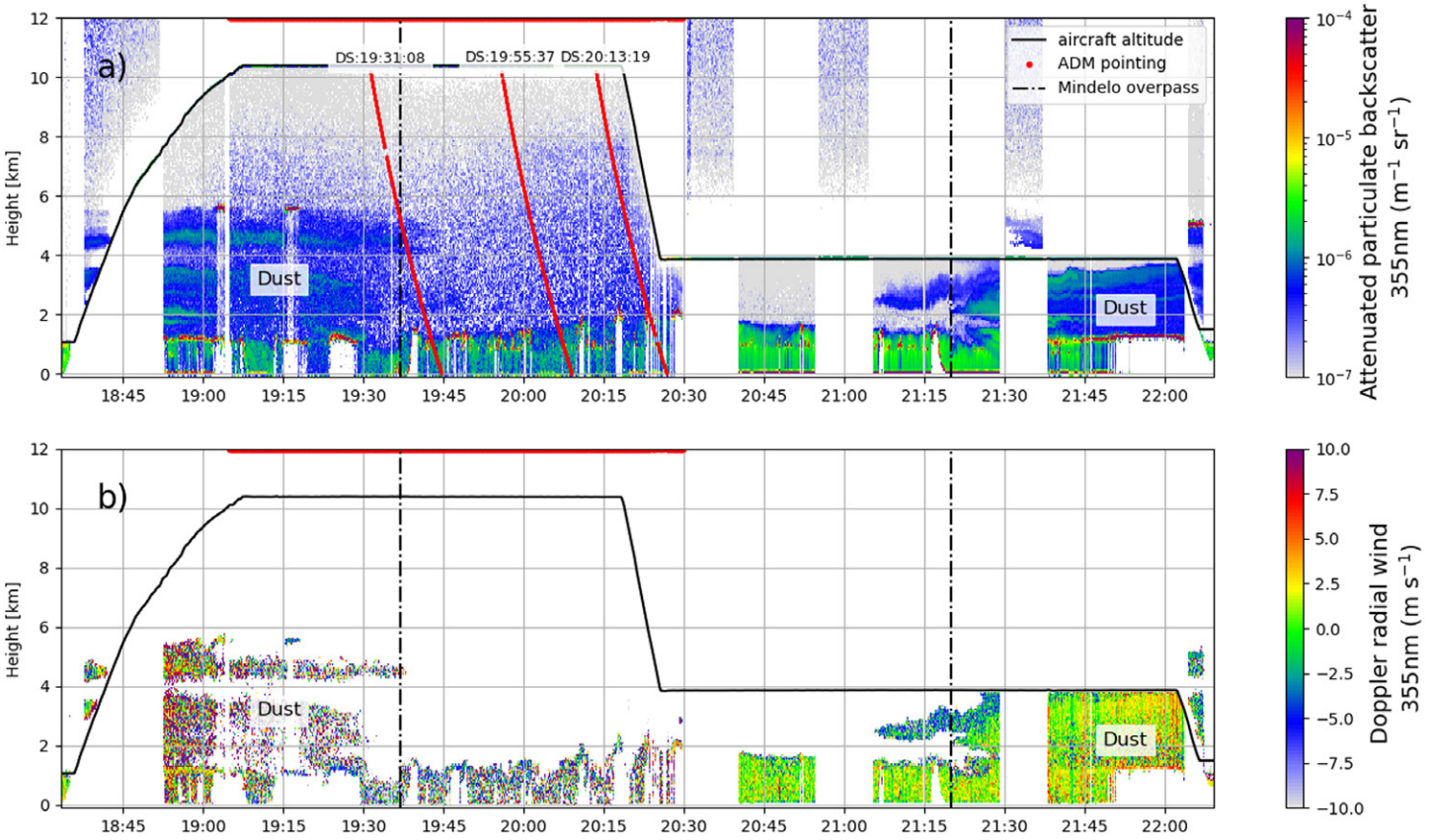

Fig. 10. LNG-derived (a) backscatter signal at 355 nm and (b) Doppler radial wind during Safire FA20 flight 11 on 17 Sep 2021. The reddish colors in (a) indicate clouds. The dust layer sampled between 1830 and 1945 UTC and between 2100 and 2200 UTC above the boundary layer appears in blue in (a). The dash–dotted lines indicate the two overpasses of Mindelo on São Vicente Island. The flight track is shown in Fig. 1 (brown track, tagged F11). The Safire FA20 was heading north during the first overpass of Mindelo and heading south during the second overpass.

layer in the early part of the flight. The upper part of the dust layer was sampled in situ when the Safire FA20 flew under its own track at 4 km MSL during the second part of the flight. Strong backscatter was obtained in the marine boundary layer and in the dust layer (especially during the second part of the flight), which allowed HLOS velocity retrievals from LNG.

Figure 11 shows an example of *Aeolus*-dropsonde HLOS winds comparison during flight F11 on 17 September during which the *Aeolus* orbit overpassed Mindelo on São Vincente Island. Comparisons are shown between the dropsonde-derived HLOS velocity and *Aeolus*-derived Mie HLOS velocity (distant from the dropsonde by 19 to 46 km) and Rayleigh HLOS velocity (~12 km away from the dropsonde). It illustrates the fairly large spread between the latest *Aeolus* L2B product (L2B12) regarding the Rayleigh HLOS velocities (between 5 and 10 m s^{-1}), but also the lack of sensitivity of *Aeolus* to dust in the lower troposphere, as *Aeolus* Mie HLOS velocities could only be derived in the marine boundary layer, likely due to sea salt aerosol. The Rayleigh HLOS wind random errors are estimated to be typically 4–5 m s^{-1}, but with high variability depending on the signal levels which vary with meteorological conditions (Rennie and Isaksen 2020). Based on a compromise between the quality of the dataset and the number of observations that pass the quality control, Rayleigh HLOS winds with an estimated error greater than 6 m s^{-1} are excluded from validation studies (Martin et al. 2021).

Further analysis using the collected data will deal with comparison statistics between *Aeolus*-derived L2B12 Rayleigh and Mie HLOS velocity products, LNG-derived and dropsonde-derived HLOS velocity products for all dedicated *Aeolus* flights during CADDIWA during September 2021. Random relative errors of the L2B Rayleigh-clear and Mie-cloudy

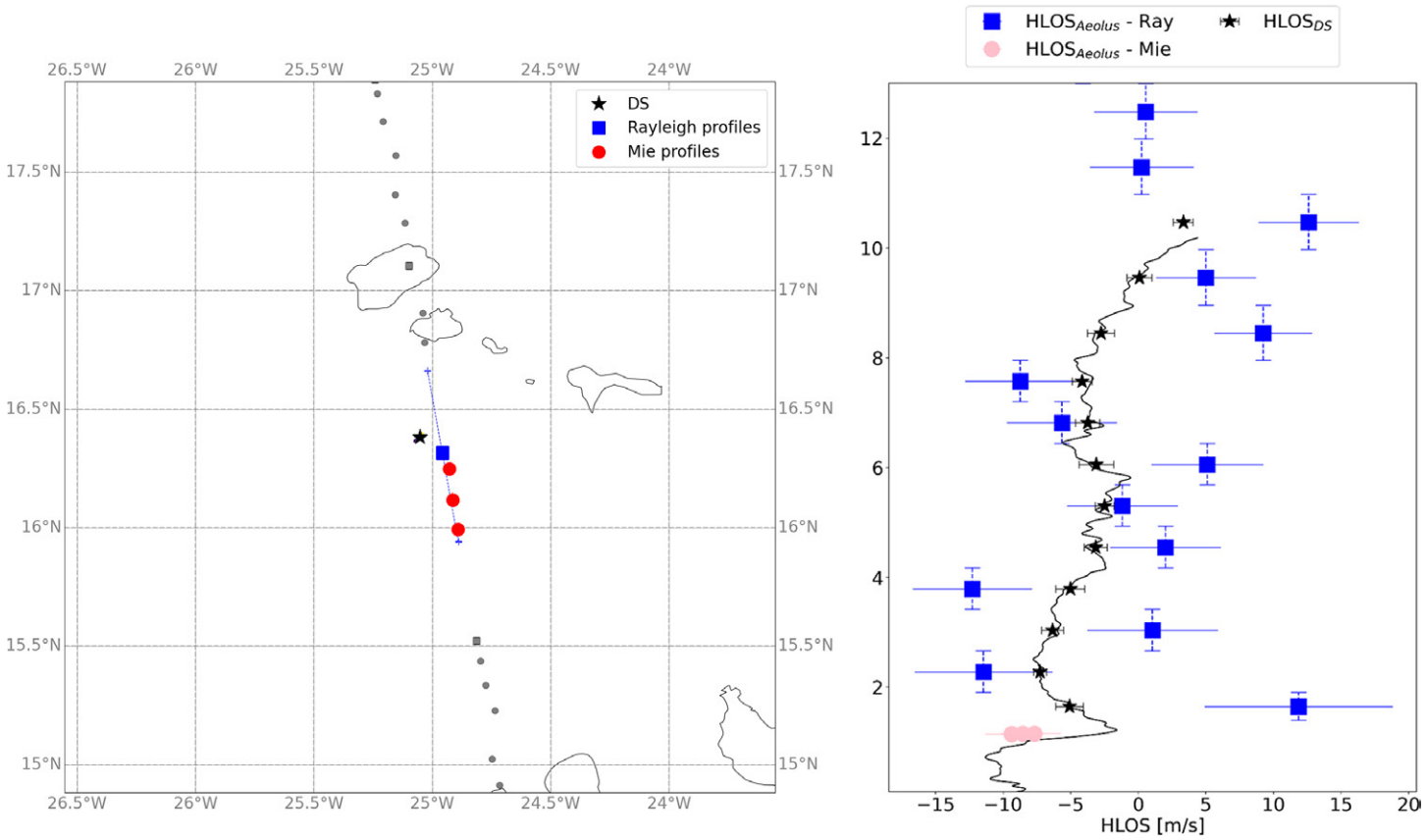

Fig. 11. (left) *Aeolus* orbit (gray squares and gray circles, indicating the location of *Aeolus* L2B Mie and Rayleigh profiles, respectively) over Cape Verde at 1936 UTC 17 Sep 2021. The blue square corresponds to the location of the *Aeolus* L2B Rayleigh wind products used for comparison with the dropsonde (black star) released south of São Vicente at the time of the *Aeolus* overpass of the Safire FA20. The red filled circles correspond to the location of the *Aeolus* L2B Mie wind products used for comparison with the dropsonde. (right) Comparison between the dropsonde-derived HLOS velocity (black symbols) and *Aeolus*-derived Mie HLOS velocity (red circles) and Rayleigh HLOS velocity (blue squares). The dropsonde was released at 1931 UTC. Error bars associated with the *Aeolus* product are also shown as colored horizontal lines.

winds derived in the tropical environment of Cape Verde with respect to both the ECMWF model background and the 2-μm heterodyne-detection Doppler wind lidar on board the Falcon aircraft during the JATAC detachment will also be analyzed.

Bio-optical measurements in the Cape Verde waters. Our optical and bio-optical measurements are the first to document the south and southwest coastal waters of the São Vicente Island to our knowledge. The bathymetry decreases very quickly as the 200-m isodepth is less than 10 km from the coast in the southwest part of the island and there is no runoffs as the annual precipitations are very low (84.2 mm). The western part of Cape Verde is known to be an oligotrophic system characterized by low macronutrient concentrations in the surface water (Ohde and Siegel 2010).

Figure 12 presents the variation of the backscattering coefficient at 532 nm, $b_{bp}(532)$ as a function of depth, and the values of the diffuse attenuation coefficient $K_d(532)$ for each station. The temporal and vertical variabilities of the backscattering coefficient $b_{bp}(532)$ are very low with values between 0.5 and 1.5 $\times$ 10^{-3} m^{-1}. For a given station, the values of $b_{bp}(532)$ are almost constant over the water column up to 30 m for the 16 stations. The phytoplankton concentration measured are very low (mean value of 0.025 mg m^{-3}, not shown here) corresponding to oligotrophic waters (Huot et al. 2008; Loisel et al. 2011). The temporal and spatial variations of $K_d(532)$ are also low with a mean value of 0.0599 m^{-1} and a standard deviation of 0.0151 m^{-1}. Those values of $K_d(532)$ correspond to very clear waters, i.e., oligotrophic waters.

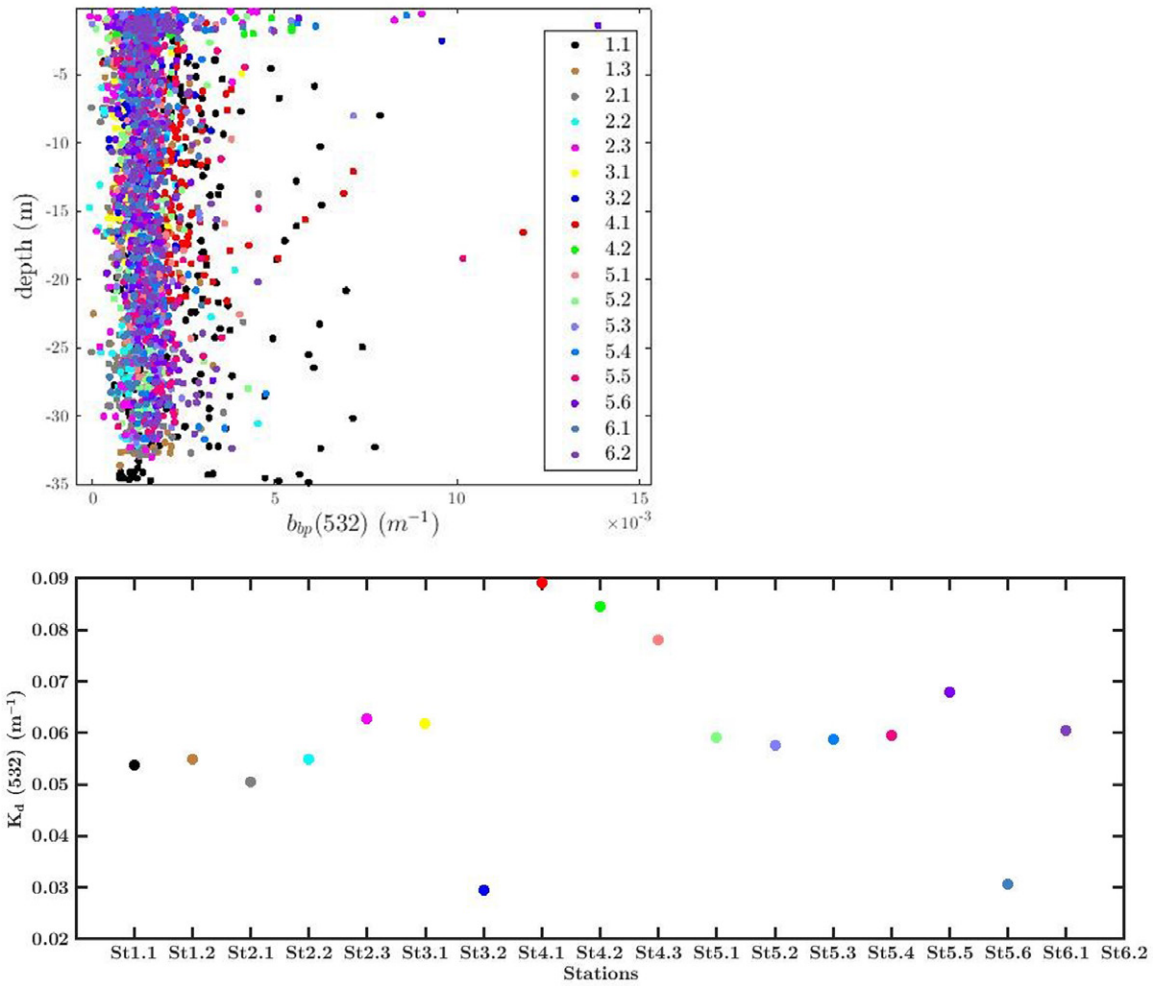

Fig. 12. (top) Variation of b_{bp}(532) as a function of depth for each station. In the legend, the first digit corresponds to the outing number (from 1 to 6) and the second digit corresponds to the station (from first to last) made during the outing. (bottom) Values of K_d(532) for each station made during the 16 stations established from the *Gamboa* boat during the six outings at sea.

For this type of waters, the UV sunlight penetrates deeper than visible sunlight, which means that the LNG and *Aeolus* lidar signals can penetrate deeply in the water column.

The subsurface lidar signal is proportional to volume backscattering coefficient from water molecules and suspended particles and hence to the hemispherical particulate backscattering parameter b_{bp}, which is an important in ocean color (as it depends on the size, type, and composition of the optically active marine particles). The attenuation coefficient of the lidar signal in water is a proxy of the diffuse attenuation coefficient K_d. Anticipated research conducted with this data will focus on the development of algorithms for processing airborne and spaceborne lidar data at 355 and 532 nm gathered around Cape Verde, as well as the validation of the lidar-derived products with seaborne subsurface observations.

Outreach and education

Participation in an international campaign such as CADDIWA is a unique opportunity for early career scientists as well as students interested in field experimentation and environmental sciences, in a key region of the globe for the understanding of atmospheric dynamics and climate variability and change.

As such, five early career scientists, an assistant professor from the University of Cape Verde in Praia (Mateus Neves Andrade), two Ph.D. students (Cédric Gacial Ngoungué Langué and Clémantyne Aubry) and two master students (Nicolau Gomes Araujo from the University

of Cape Verde in Praia, and Tanguy Jonville from Ecole Polytechnique) were invited to participate in the campaign. These early career scientists were an integral part of the CADDIWA team during the campaign and participated in the daily briefings conducted from the CADDIWA Operation Center in Sal (Fig. 13). On numerous occasions, they presented the outcome of the discussions conducted by the Meteorology and Aerosol Forecasting Groups to the broader CADDIWA audience. They were involved in the on-site data analysis during the CADDIWA hackathon organized on 23–24 September. They also were very much involved in radiosonde launch activities led by Maurus Borne (Ph.D. student at KIT) conducted at the Sal International Airport. During the campaign, Mateus Neves Andrade and Nicolau Gomes Araujo also gave interviews aired on the National Cape Verde Radio on behalf of the CADDIWA project. All the early career scientists praised this first experience in the field, and one master student, Tanguy Jonville, began his Ph.D. on the analysis of the CADDIWA cases in September 2022.

The GNSS station that was installed by Institut national de l'information géographique et forestière (IGN) in Sal during the CADDIWA detachment was set up and maintained by the two early career scientists from the University of Cape Verde in the framework of a capacity building program led by IGN. After the field campaign, the station was moved to Praia on Santiago Island, on the premises of the University of Cape Verde. Mateus Neves Andrade is now in charge of running the GNSS station under the guidance of IGN. The GNSS station served to monitor the evolution of TCWV during the NASA CPEX-CV airborne campaign that took place in September 2022 from Sal. It will also has been used for education and research purposes, with the objective to launch a new teaching program centered on tropical meteorology that does currently not exist in the University of Cape Verde Educational Program.

Finally, a series of short videos were made by ESA during the campaign that describe the payload of the Safire FA20, the lidar LNG, the radar RASTA, and the microphysical probes.

Fig. 13. The CADDIWA Operation Center in Sal. (top left) Jean-Pierre Chaboureau (standing) presenting the NHC TC track forecast facing Cyrille Flamant while Gilles Vergez and Guy Febvre (backward) are listening. (top middle left) Christophe Cadoux during a morning briefing. (top middle right) Marco Gaetani preparing the Daily Operations Report. (right) Cédric Gacial Ngoungué Langué, Azusa Takeishi, and Maurus Borne preparing the next balloon launches. (bottom left) Pierre Coutris and Guy Febvre having a good time. (bottom middle left) Tanguy Jonville, Christophe Lavaysse, and Cédric Gacial Ngoungué Langué preparing the weather briefing. (bottom middle right) Azusa Takeishi presenting the atmospheric composition briefing while Cédric Gacial Ngoungué Langué is listening. (bottom right) Pilot Dominique Duchanoy, Cyrille Flamant, and pilot Jean-François Bourdinot discussing the implementation of the airborne missions previously discussed during the CADDIWA briefing, while Marco Gaetani and Azusa Takeishi are working on the reports of the day.

They can be accessed from https://earth.esa.int/eogateway/news/jatac-caddiwa-the-french-campaign-helping-to-validate-aeolus-data-at-the-tropics. Additionally, numerous contents were posted on social media under "#CADDIWA."

Summary and outlook

The airborne measurements (9 flights with 32 scientific flight hours and 46 dropsondes) acquired during the campaign have enabled documentation of a variety of meteorological situations involving complex interactions between dynamics, aerosols, convection, and tropical disturbances. The payload on the Safire FA20, combining active and passive remote sensing as well as in situ sampling and dropsondes, was unique in the JATAC initiative. The acquired datasets are a solid foundation to answer the scientific objectives of CADDIWA with respect to understanding the role of cloud–atmospheric dynamic–dust interactions for the development of tropical storms downstream of Cape Verde. They will also allow us to better constrain the simulations which will be carried out with the help of regional climate models and NWP models, in particular to understand the impact of the various radiative effects of the aerosols on the life cycle of Tropical Perturbation Pierre Henri and TS Rose, and answer questions related to the interactions between dust and tropical waves upon which the project is built. In particular, the observations gathered during the campaign (and the accompanying modeling effort) will enable investigations about how tropical waves modulate the transport of desert dust and moisture over the tropical North Atlantic. The case of nondeveloping AEW associated with Pierre Henri will allow for investigating the impact of the dust load on the development of AEWs and other tropical waves over the ocean. The comparison between the nondeveloping AEW (Pierre Henri) and the developing AEW (Rose) cases will help with assessing how well the development of AEWs and other tropical waves are represented in state-of-the-art regional climate and NWP models. It will also permit advancement of knowledge on which of the three dust effects dominates/controls developing AEWs offshore in their transition to TSs over the Atlantic Ocean and contribute to assessment of whether this hierarchy between the three dust effects depends on the dust load and/or its vertical distribution and/or microphysics. The data acquired in particularly complex tropical scenes will also serve to validate, improve, and prepare various satellite products relating to missions of importance for the European and American space agencies.

Acknowledgments. In memoriam: Pierre Henri Flamant (21 April 1942–30 June 2020), instigator of many spaceborne missions among which was the European Space Agency Earth Explorer mission *Aeolus*. He was to participate in the CADDIWA campaign. The airborne component of CADDIWA was supported by the French national program LEFE/INSU of the Centre National de la Recherche Scientifique (CNRS), Centre National d'Etudes Spatiales (CNES), the European Space Agency (ESA), and the Institut Pierre-Simon Laplace (IPSL). The CNES/TOSCA projects funding these activities are called CADDIWA and IASI–Aerosols. Maurus Borne acknowledges Deutsche Forschungsgemeinschaft (DFG) for the funding of his Ph.D. through TRR 165 "Waves to Weather." Azusa Takeshei acknowledges CNES for the funding of her PDRA position. Airborne data were obtained using the aircraft managed by Safire, the French facility for airborne research, an infrastructure of the French National Center for Atmospheric Research (CNRS), Météo-France, and CNES. The CADDIWA project would not have been successful without the relentless efforts of the Safire staff: Aurélien Bourdon, Jean-Francois Bourdinot, Dominique Duchanoy, Thierry André, Hubert Bellec, Tetyana Jiang, and Gilles Vergez. The authors thank Oualid Aouji and Aurélien Clémençon (Division Technique de l'INSU) for their support in installing and deinstalling the LNG lidar in the Safire FA20. The boatborne component of CADDIWA was funded by CNES/TOSCA through the LidarOcean project, and by ESA through the Aeolus+ Innovation program. The crewmembers of the *Gamboa* boat. Pericles Silva, Ivanice Monteiro and Elizandro Rodrigues from the Ocean Science Mindelo Center (OSCM) for hosting the oceanic

component of the mission and for the use of their facilities. Without them, the sea campaign would not have been possible. Professor Sandra Freire of the University of Cape Verde in Praia is acknowledged for her support in the project and organizing the participation of her staff involved in the GNSS operation. Rob Koopman (ESTEC) is acknowledged for his support in the implementation of the airborne campaign with respect to the preparation of ESA space missions EarthCARE. Philippe Golloub is acknowledged for the use of the data from the AERONET/PHOTON station in Sal for Fig. 2b. The authors thank the three reviewers that helped improve the overall quality of this overview paper.

Data availability statement. CADDIWA has an open data policy. The CADDIWA database will be hosted in the Base Afrique de l'Ouest beyond African Monsoon Multidisciplinary Analyses (AMMA) Base (BAOBAB) by the French national atmospheric database AERIS (www.aeris-data.fr/). The BAOBAB portal gathers data from major field campaigns and long-term data series in West Africa, including datasets from AMMA, FENNEC, and Dynamics–Aerosol–Chemistry–Cloud Interactions in West Africa (DACCIWA). The RALI data are currently available from https://rali.aeris-data.fr/catalogue/ and the quicklooks from https://rali.aeris-data.fr/products/l2_caddiwa/. The rest of CADDIWA dataset will be publicly released in October 2023. Meanwhile, data are made available for collaborations by email request to the project lead scientist (cyrille.flamant@latmos.ipsl.fr).

References

Ansmann, A., H. Baars, M. Tesche, D. Müller, D. Althausen, R. Engelmann, T. Pauliquevis, and P. Artaxo, 2009: Dust and smoke transport from Africa to South America: Lidar profiling over Cape Verde and the Amazon rainforest. *Geophys. Res. Lett.*, **36**, L11802, https://doi.org/10.1029/2009GL037923.

——, and Coauthors, 2011: Saharan Mineral Dust Experiments SAMUM-1 and SAMUM-2: What have we learned? *Tellus*, **63B**, 403–429, https://doi.org/10.1111/j.1600-0889.2011.00555.x.

Arnault, J., and F. Roux, 2009: Case study of a developing African easterly wave during NAMMA: An energetic point of view. *J. Atmos. Sci.*, **66**, 2991–3020, https://doi.org/10.1175/2009JAS3009.1.

——, and ——, 2010a: Comparison between two case studies of developing and nondeveloping African easterly waves during NAMMA and AMMA/SOP-3: Absolute vertical vorticity budget. *Mon. Wea. Rev.*, **138**, 1420–1445, https://doi.org/10.1175/2009MWR3120.1.

——, and ——, 2010b: Failed cyclogenetic evolution of a West African monsoon perturbation observed during AMMA SOP-3. *J. Atmos. Sci.*, **67**, 1863–1883, https://doi.org/10.1175/2010JAS3203.1.

——, and ——, 2011: Characteristics of African easterly waves associated with tropical cyclogenesis in the Cape Verde Islands region in July–August–September of 2004–2008. *Atmos. Res.*, **100**, 61–82, https://doi.org/10.1016/j.atmosres.2010.12.028.

Baker, B. A., and R. P. Lawson, 2006: Improvement in determination of ice water content from two-dimensional particle imagery. Part I: Image-to-mass relationships. *J. Appl. Meteor. Climatol.*, **45**, 1282–1290, https://doi.org/10.1175/JAM2398.1; Corrigendum, **55**, 2109–2111, https://doi.org/10.1175/JAMC-D-16-0212.1.

Becker, T., P. Bechtold, and I. Sandu, 2021: Characteristics of convective precipitation over tropical Africa in storm-resolving global simulations. *Quart. J. Roy. Meteor. Soc.*, **147**, 4388–4407, https://doi.org/10.1002/qj.4185.

Behrenfeld, M. J., Y. Hu, C. A. Hostetler, G. Dall'Olmo, S. D. Rodier, J. W. Hair, and C. R. Trepte, 2013: Space-based lidar measurements of global ocean carbon stocks. *Geophys. Res. Lett.*, **40**, 4355–4360, https://doi.org/10.1002/grl.50816.

Bock, O., P. Bosser, C. Flamant, E. Doerflinger, F. Jansen, R. Fages, S. Bony, and S. Schnitt, 2021: Integrated water vapour observations in the Caribbean arc from a network of ground-based GNSS receivers during EUREC^{4}A. *Earth Syst. Sci. Data*, **13**, 2407–2436, https://doi.org/10.5194/essd-13-2407-2021.

Bou Karam, D., C. Flamant, P. Knippertz, O. Reitebuch, J. Pelon, M. Chong, and A. Dabas, 2008: Dust emissions over the Sahel associated with the West African monsoon inter-tropical discontinuity region: A representative case study. *Quart. J. Roy. Meteor. Soc.*, **134**, 621–634, https://doi.org/10.1002/qj.244.

Braun, S. A., 2010: Reevaluating the role of the Saharan air layer in Atlantic tropical cyclogenesis and evolution. *Mon. Wea. Rev.*, **138**, 2007–2037, https://doi.org/10.1175/2009MWR3135.1.

——, P. Newman, and G. M. Heymsfield, 2016: NASA's Hurricane and Severe Storm Sentinel (HS3) investigation. *Bull. Amer. Meteor. Soc.*, **97**, 2085–2102, https://doi.org/10.1175/BAMS-D-15-00186.1.

Bruneau, D., and Coauthors, 2015: 355-nm high spectral resolution airborne lidar LNG: System description and first results. *Appl. Opt.*, **54**, 8776–8785, https://doi.org/10.1364/AO.54.008776.

Burpee, R. W., 1972: The origin and structure of easterly waves in the lower troposphere of North Africa. *J. Atmos. Sci.*, **29**, 77–90, https://doi.org/10.1175/1520-0469(1972)029<0077:TOASOE>2.0.CO;2.

Carlson, T. N., and J. M. Prospero, 1972: The large-scale movement of Saharan air outbreaks over the northern equatorial Atlantic. *J. Appl. Meteor.*, **11**, 283–297, https://doi.org/10.1175/1520-0450(1972)011<0283:TLSMOS>2.0.CO;2.

Chaboureau, J.-P., and Coauthors, 2016: Fennec dust forecast intercomparison over the Sahara in June 20. *Atmos. Chem. Phys.*, **16**, 6977–6995, https://doi.org/10.5194/acp-16-6977-2016.

Chen, S.-H., Y.-C. Liu, T. R. Nathan, C. Davis, R. Torn, N. Sowa, C.-T. Chenge, and J.-P. Chen, 2015: Modeling the effects of dust-radiative forcing on the movement of Hurricane Helene (2006). *Quart. J. Roy. Meteor. Soc.*, **141**, 2563–2570, https://doi.org/10.1002/qj.2542

Churnside, J. H., B. McCarty, and X. Lu, 2013: Subsurface ocean signals from an orbiting polarization lidar. *Remote Sens.*, **5**, 3457–3475, https://doi.org/10.3390/rs5073457.

Cuesta, J., and Coauthors, 2020: Three-dimensional pathways of dust over the Sahara during summer 2011 as revealed by new Infrared Atmospheric Sounding Interferometer observations. *Quart. J. Roy. Meteor. Soc.*, **146**, 2731–2755, https://doi.org/10.1002/qj.3814.

Delanoë, J., A. Protat, O. Jourdan, J. Pelon, M. Papazzoni, R. Dupuy, J.-F. Gayet, and C. Jouan, 2013: Comparison of airborne in situ, airborne radar–lidar, and spaceborne radar–lidar retrievals of polar ice cloud properties sampled during the POLARCAT campaign. *J. Atmos. Oceanic Technol.*, **30**, 57–73, https://doi.org/10.1175/JTECH-D-11-00200.1

de Matos Valerio, A., and Coauthors, 2018: Using CDOM optical properties for estimating DOC concentrations and pCO_2 in the lower Amazon River. *Opt. Express*, **26**, A657–A677, https://doi.org/10.1364/OE.26.00A657.

DeMott, P., K. Sassen, M. R. Poellot, D. Baumgardner, D. C. Rogers, S. D. Brooks, A. J. Prenni, and S. M. Kreidenweis, 2003: African dust aerosols as atmospheric ice nuclei. *Geophys. Res. Lett.*, **30**, 1732, https://doi.org/10.1029/2003GL017410.

Dieng, A. L., S. M. Sall, L. Eymard, M. Leduc-Leballeur, and A. Lazar, 2017: Trains of African easterly waves and their relationship to tropical cyclone genesis in the eastern Atlantic. *Mon. Wea. Rev.*, **145**, 599–616, https://doi.org/10.1175/MWR-D-15-0277.1.

Dionisi, D., V. E. Brando, G. Volpe, S. Colella, and R. Santoleri, 2020: Seasonal distributions of ocean particulate optical properties from spaceborne lidar measurements in Mediterranean and Black Sea. *Remote Sens. Environ.*, **247**, 111889, https://doi.org/10.1016/j.rse.2020.111889.

Dunion, J. P., and C. S. Velden, 2004: The impact of the Saharan air layer on Atlantic tropical cyclone activity. *Bull. Amer. Meteor. Soc.*, **85**, 353–366, https://doi.org/10.1175/BAMS-85-3-353.

Dunkerton, T. J., M. T. Montgomery, and Z. Wang, 2009: Tropical cyclogenesis in a tropical wave critical layer: Easterly waves. *Atmos. Chem Phys.*, **9**, 5587–5646, https://doi.org/10.5194/acp-9-5587-2009.

Emanuel, K., and F. Zhang, 2016: On the predictability and error sources of tropical cyclone intensity forecasts. *J. Atmos. Sci.*, **73**, 3739–3747, https://doi.org/10.1175/JAS-D-16-0100.1.

Evan, T. A., J. Dunion, J. A. Foley, A. K. Heidinger, and C. S. Velden, 2006: New evidence for a relationship between Atlantic tropical cyclone activity and African dust outbreaks. *Geophys. Res. Lett.*, **33**, L19813, https://doi.org/10.1029/2006GL026408.

Fehr, T., and Coauthors, 2021: The joint ESA-NASA tropical campaign activity—Aeolus calibration/validation and science in the topics. *23rd General Assembly 2021*, Online, EGU, EGU21-15144, https://doi.org/10.5194/egusphere-egu21-15144.

Flamant, C., J.-P. Chaboureau, D. J. Parker, C. M. Taylor, J.-P. Cammas, O. Bock, F. Timouck, and J. Pelon, 2007: Airborne observations of the impact of a convective system on the planetary boundary layer thermodynamics and aerosol distribution in the inter-tropical discontinuity region of the West African monsoon. *Quart. J. Roy. Meteor. Soc.*, **133**, 1175–1189, https://doi.org/10.1002/qj.97.

Folmer, M. J., R. W. Pasken, S. Chiao, J. Dunion, and J. Halverson, 2016: Modeling studies on the formation of Hurricane Helene: The impact of GNSS dropwindsondes from the NAMMA 2006 field campaign. *Meteor. Atmos. Phys.*, **128**, 733–750, https://doi.org/10.1007/s00703-016-0452-2.

Formenti, P., and Coauthors, 2019: The Aerosols, Radiation and Clouds in southern Africa (AEROCLO-sA) field campaign in Namibia: Overview, illustrative observations and way forward. *Bull. Amer. Meteor. Soc.*, **100**, 1277–1298, https://doi.org/10.1175/BAMS-D-17-0278.1.

Grogan, D. F. P., T. R. Nathan, and S.-H. Chen, 2019: Structural changes in the African easterly jet and its role in mediating the effects of Saharan dust on

the linear dynamics of African easterly waves. *J. Atmos. Sci.*, **76**, 3351–3365, https://doi.org/10.1175/JAS-D-19-0104.1.

Herbener, S. R., S. C. van den Heever, G. G. Carrió, S. M. Saleeby, and W. R. Cotton, 2014: Aerosol indirect effects on idealized tropical cyclone dynamics. *J. Atmos. Sci.*, **71**, 2040–2055, https://doi.org/10.1175/JAS-D-13-0202.1.

Hilton, F., and Coauthors, 2012: Hyperspectral Earth observation from IASI: Five years of accomplishments. *Bull. Amer. Meteor. Soc.*, **93**, 347–370, https://doi.org/10.1175/BAMS-D-11-00027.1.

Hoarau, T., C. Barthe, P. Tulet, M. Claeys, J.-P. Pinty, O. Bousquet, J. Delanoe, and B. Vié, 2018a: Impact of the generation and activation of sea salt aerosols on the evolution of Tropical Cyclone Dumile. *J. Geophys. Res. Atmos.*, **123**, 8813–8831, https://doi.org/10.1029/2017JD028125.

——, J.-P. Pinty, and C. Barthe, 2018b: A representation of the collisional ice break-up process in the two-moment microphysics scheme LIMA v1.0 of Meso-NH. *Geosci. Model Dev.*, **11**, 4269–4289, https://doi.org/10.5194/gmd-11-4269-2018.

Hopsch, S. B., C. D. Thorncroft, and K. R. Tyle, 2010: Analysis of African easterly wave structures and their role in influencing tropical cyclogenesis. *Mon. Wea. Rev.*, **138**, 1399–1419, https://doi.org/10.1175/2009MWR2760.1.

Houze, R. A., Jr., 2004: Mesoscale convective systems. *Rev. Geophys.*, **42**, RG4003, https://doi.org/10.1029/2004RG000150.

Huot, Y., A. Morel, M. S. Twardowski, D. Stramski, and R. A. Reynolds, 2008: Particle optical backscattering along a chlorophyll gradient in the upper layer of the eastern South Pacific Ocean. *Biogeosciences*, **5**, 495–507, https://doi.org/10.5194/bg-5-495-2008.

Illingworth, A. J., and Coauthors, 2015: The EarthCARE satellite: The next step forward in global measurements of clouds, aerosols, precipitation, and radiation. *Bull. Amer. Meteor. Soc.*, **96**, 1311–1332, https://doi.org/10.1175/BAMS-D-12-00227.1.

——, and Coauthors, 2018: WIVERN: A new satellite concept to provide global in-cloud winds, precipitation, and cloud properties. *Bull. Amer. Meteor. Soc.*, **99**, 1669–1687, https://doi.org/10.1175/BAMS-D-16-0047.1.

Jenkins, G. S., and A. Pratt, 2008: Saharan dust, lightning and tropical cyclones in the eastern tropical Atlantic during NAMMA-06. *Geophys. Res. Lett.*, **35**, L12804, https://doi.org/10.1029/2008GL033979.

——, ——, and A. Heymsfield, 2008: Possible linkages between Saharan dust and tropical cyclone rain band invigoration in the eastern Atlantic during NAMMA-06. *Geophys. Res. Lett.*, **35**, L08815, https://doi.org/10.1029/2008GL034072.

——, and Coauthors, 2017: Hurricane Fred (2015): Cape Verde's first hurricane in modern times: Observations, impacts, and lessons learned. *Bull. Amer. Meteor. Soc.*, **98**, 2603–2618, https://doi.org/10.1175/BAMS-D-16-0222.1.

Jones, C., N. Mahowald, and C. Luo, 2004: Observational evidence of African desert dust intensification of easterly waves. *Geophys. Res. Lett.*, **31**, L17208, https://doi.org/10.1029/2004GL020107.

Jury, M. R., and M. J. Santiago, 2010: Composite analysis of dust impacts on African easterly waves in the Moderate Resolution Imaging Spectrometer era. *J. Geophys. Res.*, **115**, D16213, https://doi.org/10.1029/2009JD013612.

Karyampudi, V. M., and T. N. Carlson, 1988: Analysis and numerical simulations of the Saharan air layer and its effect on easterly wave disturbances. *J. Atmos. Sci.*, **45**, 3102–3136, https://doi.org/10.1175/1520-0469(1988)045<3102:AANSOT>2.0.CO;2.

——, and H. F. Pierce, 2002: Synoptic-scale influence of the Saharan air layer on tropical cyclogenesis over the eastern Atlantic. *Mon. Wea. Rev.*, **130**, 3100–3128, https://doi.org/10.1175/1520-0493(2002)130<3100:SSIOTS>2.0.CO;2.

——, and Coauthors, 1999: Validation of the Saharan dust plume conceptual model using lidar, Meteosat, and ECMWF data. *Bull. Amer. Meteor. Soc.*, **80**, 1045–1076, https://doi.org/10.1175/1520-0477(1999)080<1045:VOTSDP>2.0.CO;2.

Knap, A., A. Michaels, A. Close, H. Ducklow, and A. Dickson, Eds., 1996: Protocols for the Joint Global Ocean Flux Study (JGOFS) core measurements. JGOFS Rep. 19, 210 pp.

Knippertz, P., and M. C. Todd, 2010: The central west Saharan dust hotspot and its relation to African easterly waves and extratropical disturbances. *J. Geophys. Res.*, **115**, D12117, https://doi.org/10.1029/2009JD012819.

——, and ——, 2012: Mineral dust aerosols over the Sahara: Meteorological controls on emission and transport and implications for modeling. *Rev. Geophys.*, **50**, RG1007, https://doi.org/10.1029/2011RG000362.

Kocha, C., P. Tulet, J.-P. Lafore, and C. Flamant, 2013: The importance of the diurnal cycle of aerosol optical depth in West Africa. *Geophys. Res. Lett.*, **40**, 785–790, https://doi.org/10.1002/grl.50143.

Lac, C., and Coauthors, 2018: Overview of the Meso-NH model version 5.4 and its applications. *Geosci. Model Dev.*, **11**, 1929–1969, https://doi.org/10.5194/gmd-11-1929-2018.

Landsea, C. W., 1993: A climatology of intense (or major) Atlantic hurricanes. *Mon. Wea. Rev.*, **121**, 1703–1713, https://doi.org/10.1175/1520-0493(1993)121<1703:ACOIMA>2.0.CO;2.

——, 2015: Comments on "Monitoring and understanding trends in extreme storms: State of knowledge." *Bull. Amer. Meteor. Soc.*, **96**, 1175–1176, https://doi.org/10.1175/BAMS-D-13-00211.1.

——, and J. P. Cangialosi, 2018: Have we reached the limits of predictability for tropical cyclone track forecasting? *Bull. Amer. Meteor. Soc.*, **99**, 2237–2243, https://doi.org/10.1175/BAMS-D-17-0136.1.

Lavaysse, C., J.-P. Chaboureau, and C. Flamant, 2011: Dust impact on the West African heat low in summertime. *Quart. J. Roy. Meteor. Soc.*, **137**, 1227–1240, https://doi.org/10.1002/qj.844.

Liang, M., J. C. L. Chan, J. Xu, and M. Yamaguchi, 2021: Numerical prediction of tropical cyclogenesis Part I: Evaluation of model performance. *Quart. J. Roy. Meteor. Soc.*, **147**, 1626–1641, https://doi.org/10.1002/qj.3987.

Liu, Q., X. Cui, C. Jamet, X. Zhu, Z. Mao, P. Chen, J. Bai, and D. Liu, 2020: A semi-analytic Monte Carlo simulator for spaceborne oceanic lidar: Framework and preliminary results. *Remote Sens.*, **12**, 2820, https://doi.org/10.3390/rs12172820.

Loisel, H., and Coauthors, 2011: Characterization of the bio-optical anomaly and diurnal variability of particulate matter, as seen from scattering and backscattering coefficients, in ultra-oligotrophic eddies of the Mediterranean Sea. *Biogeosciences*, **8**, 3295–3317, https://doi.org/10.5194/bg-8-3295-2011.

Lu, X., Y. Hu, C. Trepte, S. Zeng, and J. H. Churnside, 2014: Ocean subsurface studies with the CALIPSO spaceborne lidar. *J. Geophys. Res. Oceans*, **119**, 4305–4317, https://doi.org/10.1002/2014JC009970.

Luo, H., and Y. Han, 2021: Impacts of the Saharan air layer on the physical properties of the Atlantic tropical cyclone cloud systems: 2003–2019. *Atmos. Chem. Phys.*, **21**, 15171–15184, https://doi.org/10.5194/acp-21-15171-2021.

Lux, O., C. Lemmerz, F. Weiler, U. Markensteiner, B. Witschas, S. Rahm, A. Geiß, and O. Reitebuch, 2020: Intercomparison of wind observations from the European Space Agency's Aeolus satellite mission and the ALADIN Airborne Demonstrator. *Atmos. Meas. Tech.*, **13**, 2075–2097, https://doi.org/10.5194/amt-13-2075-2020.

Marsham, J. H., P. Knippertz, N. S. Dixon, D. J. Parker, and G. M. S. Lister, 2011: The importance of the representation of deep convection for modeled dust-generating winds over West Africa during summer. *Geophys. Res. Lett.*, **38**, L16803, https://doi.org/10.1029/2011GL048368.

Martin, A., M. Weissmann, O. Reitebuch, M. Rennie, A. Geiß, and A. Cress, 2021: Validation of Aeolus winds using radiosonde observations and numerical weather prediction model equivalents. *Atmos. Meas. Tech.*, **14**, 2167–2183, https://doi.org/10.5194/amt-14-2167-2021.

McConnell, C. L., E. J. Highwood, H. Coe, P. Formenti, B. Anderson, S. Osborne, S. Nava, and G. Chen, 2008: Seasonal variations of the physical and optical characteristics of Saharan dust: Results from the Dust Outflow and Deposition to the Ocean (DODO) experiment. *J. Geophys. Res.*, **113**, D14S05, https://doi.org/10.1029/2007JD009606.

Menut, L., 2023: Variability and combination as an ensemble of mineral dust forecasts during the 2021 CADDIWA experiment using the WRF 3.7.1 and

CHIMERE v2020r3 models. *Geosci. Model Dev.*, **16**, 4265–4281, https://doi.org/10.5194/gmd-16-4265-2023.

——, and Coauthors, 2021: The CHIMERE v2020r1 online chemistry-transport model. *Geosci. Model Dev.*, **14**, 6781–6811, https://doi.org/10.5194/gmd-14-6781-2021.

Mlawer, E. J., S. J. Taubman, P. D. Brown, M. J. Iacono, and S. A. Clough, 1997: Radiative transfer for inhomogeneous atmospheres: RRTM, a validated correlated-k model for the longwave. *J. Geophys. Res.*, **102**, 16 663–16 682, https://doi.org/10.1029/97JD00237.

Nathan, T. R., D. F. P. Grogan, and Chen, S.-H., 2019: Saharan dust transport during the incipient growth phase of African easterly waves. *Geosciences*, **9**, 388, https://doi.org/10.3390/geosciences9090388.

N'Datchoh, E. T., I. Diallo, A. Konaré, S. Silué, K. O. Ogunjobi, A. Diedhiou, and M. Doumbia, 2018: Dust induced changes on the West African summer monsoon features. *Int. J. Climatol.*, **38**, 452–466, https://doi.org/10.1002/joc.5187.

NOAA, 2021: Hurricane costs. NOAA, https://coast.noaa.gov/states/fast-facts/hurricane-costs.html.

Nowottnick, E. P., P. R. Colarco, S. A. Braun, D. O. Barahona, A. da Silva, D. L. Hlavka, M. J. McGill, and J. R. Spackman, 2018: Dust impacts on the 2012 Hurricane Nadine track during the NASA HS3 field campaign. *J. Atmos. Sci.*, **75**, 2473–2489, https://doi.org/10.1175/JAS-D-17-0237.1.

Ohde, T., and H. Siegel, 2010: Biological response to coastal upwelling and dust deposition in the area off northwest Africa. *Cont. Shelf Res.*, **30**, 1108–1119, https://doi.org/10.1016/j.csr.2010.02.016.

Pasch, R. J., L. A. Avila, and J.-G. Jiing, 1998: Atlantic tropical systems of 1994 and 1995: A comparison of a quiet season to a near-record-breaking one. *Mon. Wea. Rev.*, **126**, 1106–1123, https://doi.org/10.1175/1520-0493(1998)126<1106:ATSOAA>2.0.CO;2.

Pergaud, J., V. Masson, S. Malardel, and F. Couvreux, 2009: A parameterization of dry thermals and shallow cumuli for mesoscale numerical weather prediction. *Bound.-Layer Meteor.*, **132**, 83–106, https://doi.org/10.1007/s10546-009-9388-0.

Pinty, J.-P., and P. Jabouille, 1998: A mixed-phase cloud parameterization for use in a mesoscale non-hydrostatic model: Simulations of a squall line and of orographic precipitations. *Proc. Conf. on Cloud Physics*, Everett, WA, Amer. Meteor. Soc., 217–220.

Price, H. C., and Coauthors, 2018: Atmospheric ice-nucleating particles in the dusty tropical Atlantic. *J. Geophys. Res. Atmos.*, **123**, 2175–2193, https://doi.org/10.1002/2017JD027560.

Ramanathan, V., and Coauthors, 2007: Atmospheric brown clouds: Hemispherical and regional variations in long-range transport, absorption, and radiative forcing. *J. Geophys. Res.*, **112**, D22S21, https://doi.org/10.1029/2006JD008124.

Redelsperger, J.-L., C. D. Thorncroft, A. Diedhiou, T. Lebel, D. J. Parker, and J. Polcher, 2006: African Monsoon Multidisciplinary Analysis: An international research project and field campaign. *Bull. Amer. Meteor. Soc.*, **87**, 1739–1746, https://doi.org/10.1175/BAMS-87-12-1739.

Reed, K. A., J. T. Bacmeister, J. J. A. Huff, X. Wu, S. C. Bates, and N. A. Rosenbloom, 2019: Exploring the impact of dust on North Atlantic hurricanes in a high-resolution climate model. *Geophys. Res. Lett.*, **46**, 1105–1112, https://doi.org/10.1029/2018GL080642.

Reed, R. J., D. C. Norquist, and E. E. Recker, 1977: The structure and properties of African wave disturbances as observed during phase III of GATE. *Mon. Wea. Rev.*, **105**, 317–333, https://doi.org/10.1175/1520-0493(1977)105<0317:TSAPOA>2.0.CO;2.

Reinares-Martínez, I., and J.-P. Chaboureau, 2018: Precipitation and mesoscale convective systems: Radiative impact of dust over northern Africa. *Mon. Wea. Rev.*, **146**, 3011–3029, https://doi.org/10.1175/MWR-D-18-0103.1.

Rennie, M., and L. Isaksen, 2020: The NWP impact of Aeolus level-2B winds at ECMWF. ECMWF Tech. Memo. 864, 110 pp., https://doi.org/10.21957/alift7mhr.

Russell, J. O., A. Aiyyer, J. D. White, and W. Hannah, 2017: Revisiting the connection between African easterly waves and Atlantic tropical cyclogenesis. *Geophys. Res. Lett.*, **44**, 587–595, https://doi.org/10.1002/2016GL071236.

Ryder, C. L., and Coauthors, 2018: Coarse-mode mineral dust size distributions, composition and optical properties from AER-D aircraft measurements over the tropical eastern Atlantic. *Atmos. Chem. Phys.*, **18**, 17 225–17 257, https://doi.org/10.5194/acp-18-17225-2018.

Schwendike, J., and S. Jones, 2010: Convection in an African easterly wave over West Africa and the eastern Atlantic: A model case study of Helene (2006). *Quart. J. Roy. Meteor. Soc.*, **136**, 364–396, https://doi.org/10.1002/qj.566.

Stoffelen, A., and Coauthors, 2005: The Atmospheric Dynamics Mission for global wind field measurement. *Bull. Amer. Meteor. Soc.*, **86**, 73–88, https://doi.org/10.1175/BAMS-86-1-73.

Tanré, D., and Coauthors, 2003: Measurement and modeling of the Saharan dust radiative impact: Overview of the Saharan Dust Experiment (SHADE). *J. Geophys. Res.*, **108**, 8574, https://doi.org/10.1029/2002JD003273.

Thorncroft, C. D., and K. Hodges, 2001: African easterly wave variability and its relationship to Atlantic tropical cyclone activity. *J. Climate*, **14**, 1166–1179, https://doi.org/10.1175/1520-0442(2001)014<1166:AEWVAI>2.0.CO;2.

Tuccella, P., L. Menut, R. Briant, A. Deroubaix, D. Khvorostyanov, S. Mailler, G. Siour, and S. Turquety, 2019: Implementation of aerosol-cloud interaction within WRF-CHIMERE online coupled model: Evaluation and investigation of the indirect radiative effect from anthropogenic emission reduction on the Benelux Union. *Atmosphere*, **10**, 20, https://doi.org/10.3390/atmos10010020.

Vogel, P., P. Knippertz, A. H. Fink, A. Schlueter, and T. Gneiting, 2018: Skill of global raw and postprocessed ensemble predictions of rainfall over northern tropical Africa. *Wea. Forecasting*, **33**, 369–388, https://doi.org/10.1175/WAF-D-17-0127.1

Washington, R., and M. C. Todd, 2005: Atmospheric controls on mineral dust emission from the Bodélé depression, Chad: The role of the low level jet. *Geophys. Res. Lett.*, **32**, L17701, https://doi.org/10.1029/2005GL023597.

Weinzierl, B., and Coauthors, 2017: The Saharan Aerosol Long-Range Transport and Aerosol–Cloud-Interaction Experiment: Overview and selected highlights. *Bull. Amer. Meteor. Soc.*, **98**, 1427–1451, https://doi.org/10.1175/BAMS-D-15-00142.1.

Yin, Y., and L. Chen, 2007: The effects of heating by transported dust layers on cloud and precipitation: A numerical study. *Atmos. Chem. Phys.*, **7**, 3497–3505, https://doi.org/10.5194/acp-7-3497-2007.

Zender, C. S., H. Bian, and D. Newman, 2003: Mineral Dust Entrainment and Deposition (DEAD) model: Description and 1990s dust climatology. *J. Geophys. Res.*, **108**, 4416, https://doi.org/10.1029/2002JD002775.

Zhao, C., X. Liu, L. R. Leung, B. Johnson, S. A. McFarlane, W. I. Gustafson Jr., J. D. Fast, and R. Easter, 2010: The spatial distribution of mineral dust and its shortwave radiative forcing over North Africa: Modeling sensitivities to dust emissions and aerosol size treatments. *Atmos. Chem. Phys.*, **10**, 8821–8838, https://doi.org/10.5194/acp-10-8821-2010.

——, ——, ——, and S. Hagos, 2011: Radiative impact of mineral dust on monsoon precipitation variability over West Africa. *Atmos. Chem. Phys.*, **11**, 1879–1893, https://doi.org/10.5194/acp-11-1879-2011.

Zipser, E. J., and Coauthors, 2009: The Saharan air layer and the fate of African easterly waves—NASA's AMMA field study of tropical cyclogenesis. *Bull. Amer. Meteor. Soc.*, **90**, 1137–1156, https://doi.org/10.1175/2009BAMS2728.1.